Mon. Not. R. Astron. Soc. **358,** 1453–1471 (2005) doi:10.1111/j.1365-2966.2005.08863.x

A *Chandra* X-ray survey of nearby dwarf starburst galaxies – II. Starburst properties and outflows

Jürgen Ott,[1⋆]† Fabian Walter[2]† and Elias Brinks[3,4]†

[1]*CSIRO, Australia Telescope National Facility, Cnr Vimiera & Pembroke Roads, Marsfield, NSW 2112, Australia*
[2]*Max-Planck-Institut für Astronomie, Königstuhl 17, 69117 Heidelberg, Germany*
[3]*Instituto Nacional de Astrofísica Óptica y Electrónica, Apartado Postal 51 y 216, Puebla, Pue 72000, Mexico*
[4]*Centre for Astrophysics Research, University of Hertfordshire, College Lane, Hatfield AL10 9AB*

Accepted 2005 January 21. Received 2005 January 18

ABSTRACT

We present a comprehensive comparison of the X-ray properties of a sample of eight dwarf starburst galaxies observed with *Chandra* (I Zw 18, VII Zw 403, NGC 1569, NGC 3077, NGC 4214, NGC 4449, NGC 5253 and He 2–10). In Paper I, we presented in detail the data reduction and analysis of the individual galaxies. For the unresolved X-ray sources, we find the following: point sources are in general located close to bright H II regions, rims of superbubbles or young stellar clusters. The number of X-ray point sources appears to be a function of the current star formation (SF) rate and the blue luminosity of the hosts. Ultraluminous X-ray sources (ULXs) are only found in those dwarf galaxies that are currently interacting. The power-law (PL) index of the combined cumulative X-ray point-source luminosity function is $\alpha = 0.24 \pm 0.06$, shallower than that of more massive starburst galaxies ($\alpha = 0.4$ –0.8) and of non-starburst galaxies ($\alpha \sim 1.2$). For those galaxies showing extended X-ray emission (six out of the eight galaxies), we derive the following: superwinds develop along the steepest gradient of the H I distribution with volume densities of 0.02–0.06 cm^{-3}, pressures of 1–3 $\times\ 10^5$ K cm^{-3}, thermal energies of 2–30 $\times\ 10^{54}$ erg and hot gas masses of 2–20 $\times\ 10^6\ \mathrm{M}_\odot$ ($\sim$1 per cent of the H I masses). On global scales, the distribution of the X-ray emission looks remarkably similar to that seen in Hα (comparing azimuthal averages); locally, however, their distribution is clearly distinct in many cases, which can be explained by the different emission mechanisms (forward versus reverse shocks). Mass loading of order 1 to 5 is required to explain the differences between the amount of hot gas and the modelled mass loss from massive stars. The metallicity of the dwarf galaxies correlates with the diffuse X-ray luminosity and anticorrelates with the cooling time of the hot gas. The diffuse X-ray luminosity is also a function of the current star formation rate (SFR). The mechanical luminosities of the developing superwinds are energetic enough to overcome the gravitational potentials of their host galaxies. This scenario is supported by the overpressures of the hot gas compared with the ambient interstellar medium (ISM). Extended H I envelopes such as tidal tails, however, may delay outflows on time-scales exceeding those of the cooling time of the hot gas.

Key words: ISM: jets and outflows – galaxies: dwarf – intergalactic medium – galaxies: starburst – X-rays: galaxies – X-rays: ISM.

1 INTRODUCTION

Starburst phases in galaxies dump a huge amount of mechanical and thermal energy into the interstellar medium (ISM) of their hosts via stellar winds and supernovae (SNe; see, e.g. the models of Leitherer et al. 1999). The mechanical energy that is deposited creates shocks in the ambient medium: a forward shock ionizes the ISM to temperatures of $\sim 10^{4-5}$ K, and is visible as diffuse emission in Hα and other optical spectral lines. A reverse shock thermalizes the stellar ejecta to temperatures of $\sim 10^{6-8}$ K, which gives rise to X-rays (e.g. Castor, Weaver & McCray 1975; Weaver et al. 1977; Heckman 2002; Strickland et al. 2002). This coronal gas is characterized by high pressures, which are capable of pushing material to the halo.

⋆Bolton Fellow.
†E-mail: Juergen.Ott@csiro.au (JO); walter@mpia.de (FW); ebrinks@star.herts.ac.uk (EB)

If the gravitational potential is shallow and the cooler gas in the halo is not very extended, the material is able to ultimately overcome the gravitational potential of the host and the hydrodynamical drag of the surrounding gas. Eventually, the hot gas escapes into the intergalactic medium (IGM; Mac Low & Ferrara 1999; Ferrara & Tolstoy 2000; Silich & Tenorio-Tagle 2001). To first order, the end products of massive star formation (SF) are oblivious to their environment and release the same amount of energy whether SF has taken place in a spiral or in a dwarf galaxy. Dwarf galaxies, however, have a much shallower gravitational potential and outflows can be established more easily. As metals are produced in high-mass stars, the hot gas carries freshly produced heavy elements with it and distributes them over the entire galaxy and/or the IGM (e.g. Silich et al. 2001b). In particular, the energy input is mainly provided by Type II SNe, which predominantly release α elements. Iron is efficiently produced in Type Ia SNe but they occur with a substantial time delay (see, e.g. Matteucci & Recchi 2001). For this reason, the α/Fe ratio in the outflow is predicted to be higher than solar.

This picture has three important implications. First of all, it could explain why dwarf galaxies have a much lower metallicity ($Z \simeq 1/10$ solar, see, e.g. Skillman, Kennicutt & Hodge 1989) as compared with larger spirals ($Z \simeq$ solar). Secondly, if a starburst is strong enough, it can blow away all of its ISM. In that case, the galaxy is not able to further form stars and eventually fades. Thirdly, the gas that is expelled to the IGM pollutes it with heavy elements. This might have been especially important at large look-back times. In cold dark matter cosmologies, spiral galaxies form by mergers of smaller constituents. Dwarf galaxies formed relatively early and may have quickly polluted the IGM by galactic superwinds before larger systems got assembled. As a result of the larger number of small systems and a higher merging rate, which triggers SF, the removal of metal-enriched gas in dwarf galaxies by the energetic input of SNe and stellar winds may have been more common in the past, and may have influenced the formation and evolution of galaxies in general.

This prompted us to embark on a detailed study with the *Chandra X-ray Observatory* (*CXO*) of a sample of eight dwarf galaxies that are undergoing a starburst. The aim of our study is to try to trace the hot gas in these systems, determine its extent, measure the relative abundance of α elements over iron and assess the likelihood that this hot gas will escape the galaxy. In Ott, Walter & Brinks (2005, hereafter referred to as Paper I), we presented the sample and a detailed description of our data reduction techniques. We detected 55 unresolved sources that are likely related to the galaxies and we presented fits to their individual spectra. Six of the dwarf galaxies have diffuse X-ray emission and we derived such fundamental parameters as their X-ray luminosity, the temperature, and the α Fe element abundance ratio of the gas.

This paper is dedicated to a comparison of the X-ray characteristics of the dwarf galaxies in our sample and of any correlations of their X-ray with other properties. In Section 2, we summarize the general properties of the galaxies in our sample. This is followed in Section 3 by a discussion of the morphologies of the different components (X-ray, optical, Hα and H I). In Section 4, the point-source population in the galaxies is discussed according to their locations in the galaxies, their spectral properties and their correlations with SF tracers. In this section, we also present our interpretation of the point-source luminosity function. The X-ray properties of the diffuse, coronal gas are evaluated and compared in Section 5. Correlations of those properties with quantities derived at other wavelengths are presented in Section 6, followed by a discussion on the probability of outflows in Section 7. Section 8 summarizes our results.

2 GENERAL PROPERTIES OF THE SAMPLE GALAXIES

In this section, we compile complementary data on the galaxies in our sample taken from the literature. The sample consists of eight dwarf starburst galaxies: I Zw 18, VII Zw 403, NGC 1569, NGC 3077, NGC 4214, NGC 4449, NGC 5253 and He 2–10 (see Paper I). We took care, as much as possible, to present the data in a homogeneous manner. We checked the literature for optical, far-infrared (FIR) and H I properties of our sample. The data were selected to only include directly observed parameters such as, e.g. fluxes. In Table 1, we list distances and optical data; the distance (D) to the objects is listed in column 2. Columns 3 and 4 give the total blue magnitude corrected for Galactic extinction and inclination ($m_{\rm B}^0$) as well as the K-band magnitude. The diameter at the 25 mag arcsec^{-2} isophote (d_{25}) is tabulated in column 5 and the Hα fluxes ($F_{\rm H\alpha}$) in column 6. Finally, the oxygen abundance ($12 + \log$ [O/H]) is given in column 7. The last column presents references to the literature that was used to retrieve the information listed in columns 2 to 7. The columns in Table 2 show the following: column 2, H I flux ($F_{\rm HI}$); columns 3 and 4, FIR 60- and 100-μm flux densities ($S_{60\,\mu{\rm m}}$ and $S_{100\,\mu{\rm m}}$); column 5, the heliocentric radial systemic velocities ($v_{\rm hel}$) as derived from radio measurements. Again, the last column

Table 1. Distances and optical properties of the galaxy sample.

Galaxy	D	$m_{\rm B}^0$	$m_{\rm K_s}$	d_{25}	$F_{\rm H\alpha}$	$12 + \log$(O/H)	References
	(Mpc)	(mag)	(mag)	(arcmin)	(erg s^{-1} cm^{-2})		
(1)	(2)	(3)	(4)	(5)	(6)	(7)	(8)
I Zw 18	12.6	16.47 ± 0.17	...	0.41 ± 0.11	3.26×10^{-13}	7.16	1, 2, -, 2, 3, 4
VII Zw4 403	4.5	15.74 ± 0.38	...	0.93 ± 0.13	1.95×10^{-11}	7.73 ± 0.01	5, 2, -, 2, 6, 7
NGC 1569	2.2	8.29 ± 0.32	7.86 ± 0.02	3.24 ± 0.11	8.28×10^{-11}	8.22 ± 0.07	8, 2, 9, 2, 10, 11
NGC 3077	3.6	10.19 ± 0.11	7.30 ± 0.02	4.90 ± 0.60	3.75×10^{-12}	8.90	12, 2, 9, 2, 13, 11
NGC 4214	2.9	10.17 ± 0.21	7.91 ± 0.05	8.91 ± 1.32	1.47×10^{-11}	8.28 ± 0.08	14, 2, 9, 2, 15, 16
NGC 4449	3.9	9.65 ± 0.62	7.25 ± 0.04	5.62 ± 0.29	2.03×10^{-11}	8.31 ± 0.07	17, 2, 9, 2, 10, 11
NGC 5253	3.3	9.77 ± 0.40	8.29 ± 0.03	4.79 ± 0.11	1.70×10^{-11}	8.23 ± 0.01	18, 2, 9, 2, 19, 11
He 2–10	9.0	11.97 ± 0.01	9.00 ± 0.02	1.82 ± 0.12	3.50×10^{-12}	8.93	20, 2, 9, 2, 21, 22

References: (1) Östlin (2000); (2) Paturel et al. (1997); (3) Cannon at al. (2002); (4) Guseva, Izotov & Thuan (2000); (5) Lynds et al. (1998); (6) Silich et al. (2002); (7) Izotov, Thuan & Lipovetsky (1997); (8) Israel (1988); (9) 2MASS Atlas, Jarrett et al. (2003); (10) Hunter, Hawley & Gallagher (1993); (11) Martin (1997); (12) Freedman et al. (1994); (13) Walter et al. (2002); (14) Maíz-Apellániz, Cieza & MacKenty (2002); (15) Martin (1998); (16) Kobulnicky & Skillman (1996); (17) Hunter et al. (1998); (18) Gibson et al. (2000); (19) Marlowe et al. (1997); (20) Vacca & Conti (1992); (21) Johnson et al. (2000); (22) Kobulnicky, Kennicutt & Pizagno (1999).

Table 2. H I and far-infrared (FIR) properties of the galaxy sample.

Galaxy	$F_{\rm H\,I}$ (Jy km s^{-1})	$S_{60\,\mu m}$ (Jy)	$S_{100\,\mu m}$ (Jy)	$v_{\rm hel}$ (km s^{-1})	References
(1)	(2)	(3)	(4)	(5)	(6)
I Zw 18	1.19	...	...	752 ± 8	1,–,–, 2
VII Zw 403	14.41	0.38 ± 0.04	0.90 ± 0.17	-93 ± 6	3, 4, 4, 2
NGC 1569	96.30 ± 17.50	46.48 ± 5.11	51.71 ± 10.86	-90 ± 11	5, 4, 4, 2
NGC 3077	42.13	14.80 ± 1.18	25.11 ± 2.51	14 ± 6	6, 7, 7, 2
NGC 4214	320 ± 2	17.87 ± 0.08	29.04 ± 0.11	291 ± 3	8, 9, 9, 2
NGC 4449	41.72	36.00 ± 3.00	73.00 ± 20.00	202 ± 7	10, 4, 4, 2
NGC 5253	34.80 ± 5.10	31.24 ± 3.44	29.78 ± 3.28	403 ± 13	11, 4, 4, 2
He 2-10	17.09 ± 1.04	24.08 ± 2.65	26.40 ± 2.90	874 ± 9	12, 4, 4, 2

References: (1) van Zee et al. (1998, (H I-A in their notation); (2) Bottinelli et al. (1990); (3) Tully et al. (1981); (4) Beichman et al. (1988); (5) Israel (1988); (6) integrated over optical counterpart, Walter et al. (2002); (7) Hunter et al. (1986); (8) Huchtmeier & Seiradakis (1985); (9) Soifer et al. (1989); (10) based on the H I image of Hunter et al. (1999), including the prominent H I ring around the optical counterpart; (11) Huchtmeier & Richter (1989); (12) Sauvage, Thuan & Lagage (1997).

Table 3. Derived quantities of the galaxy sample.

Galaxy	$M_{\rm B}$ (mag)	$L_{\rm B}$ ($10^8\,L_{\rm B\odot}$)	$L_{\rm K}$ ($10^8\,L_{\rm K\odot}$)	Z (solar)	$L_{\rm H\alpha}$ (10^{38} erg s^{-1})	$SFR_{\rm H\alpha}$ (M$_\odot$ yr^{-1})
(1)	(2)	(3)	(4)	(5)	(6)	(7)
I Zw 18	−14.01 ± 0.17	0.65 ± 0.10	...	0.02	61.9 ± 18.6	0.06 ± 0.02
VII Zw4 03	−12.53 ± 0.3	0.16 ± 0.07	...	0.07	472.5 ± 10.0	0.42 ± 0.01
NGC 1569	−18.42 ± 0.32	36.98 ± 11.00	7.45 ± 0.13	0.21	479.5 ± 143.9	0.43 ± 0.13
NGC 3077	−17.59 ± 0.11	17.22 ± 1.70	44.06 ± 0.81	1.00	58.2 ± 17.5	0.05 ± 0.02
NGC 4214	−17.14 ± 0.21	11.38 ± 0.35	12.36 ± 0.58	0.25	147.9 ± 44.4	0.13 ± 0.04
NGC 4449	−18.31 ± 0.62	33.42 ± 20.00	40.93 ± 1.53	0.26	369.4 ± 110.8	0.32 ± 0.10
NGC 5253	−17.82 ± 0.40	21.28 ± 8.00	11.27 ± 0.31	0.21	139.4 ± 41.8	0.12 ± 0.04
He 2-10	−17.80 ± 0.01	20.89 ± 1.80	43.65 ± 0.81	1.07	339.2 ± 101.8	0.30 ± 0.09

Galaxy	M$_{\rm H\,I}$ (10^8 M$_\odot$)	$L_{\rm FIR}$ ($10^8 L_{\rm FIR,\odot}$)	$SFR_{\rm FIR}$ (M$_\odot$ yr^{-1})	$M_{\rm dust}$ (10^4 M$_\odot$)	$t_{\rm life}$ (Gyr)	$M_{\rm H\,I}/L_{\rm B}$ (M$_\odot$/$L_{\rm B\odot}$)
	(8)	(9)	(10)	(11)	(12)	(13)
I Zw 18	0.4 ± 0.01	...	...	0.4 ± 0.2[2]	0.7	0.62
VII Zw4 03	0.7 ± 0.2	0.3 ± 0.04	0.005 ± 0.001	0.5 ± 0.3	0.2	4.4
NGC 1569	1.1 ± 0.2	5.9 ± 0.7	0.102 ± 0.012	2.5 ± 0.7	0.3	0.03
NGC 3077	1.3 ± 0.4	5.8 ± 0.6	0.100 ± 0.010	5.7 ± 2.9	2.6	0.08
NGC 4214	6.4 ± 0.1	4.5 ± 1.4	0.078 ± 0.024	4.0 ± 2.0	4.9	0.6
NGC 4449	1.5 ± 0.5	17.9 ± 2.8	0.309 ± 0.048	25.7 ± 12.9	0.5	0.04
NGC 5253	0.9 ± 0.1	8.5 ± 0.8	0.147 ± 0.014	2.6 ± 1.3	0.8	0.04
He 2–10	3.3 ± 0.2	51.9 ± 5.2	0.895 ± 0.090	20.6 ± 10.3	1.1	0.16

lists the references for the data presented in columns 2 to 5. Note that the large-scale tidal tails around I Zw 18, NGC 3077 and NGC 4449 were not included in the analysis of the H I data.

The derived properties of the galaxy sample were compiled from the direct measurements given in Tables 1 and 2 and are shown in Table 3. Whenever no errors were available, we assumed a conservative 30 per cent uncertainty for the observed parameters. The absolute magnitudes $M_{\rm B}$ (column 2) were derived from the equation $m^0_{\rm B} - M_{\rm B} = 5 \log D - 5$, where the distance D is given in parsec. The errors were based on those given for $m^0_{\rm B}$. Blue luminosities $L_{\rm B}$ (column 3) were calculated via $L_{\rm B} = 10^{-0.4(M_{\rm B}-M_{\rm B\odot})}\,L_{\rm B\odot}$; following Lang (1992), we assumed an absolute blue solar magnitude of $M_{\rm B\odot} = 5.50$ mag. K-band luminosities (column 4) were derived in an analogous fashion but with $M_{\rm K\odot} = 3.33$ mag (Cox 2000). Furthermore, we used the solar oxygen abundance 12 + log(O/H) = 8.9 determined by Lambert (1978) to express the metallicity Z in solar units (column 5).

Hα luminosities (column 6) were derived from the corresponding fluxes by multiplying with the geometrical factor $4\pi D^2$. We used the conversion established by Kennicutt (1983), to obtain the Hα star formation rates (SFRs; $SFR_{\rm H\alpha}$, column 7): $SFR_{\rm H\alpha} = L_{\rm H\alpha}/(1.12 \times 10^{41}$ erg s^{-1}) M$_\odot$ yr^{-1}.

For the conversion of H I flux to the corresponding mass ($M_{\rm H\,I}$, given in column 8 of Table 3) the following equation is used: $M_{\rm H\,I} = 2.36 \times 10^5 D^2 F_{\rm H\,I}$ (Rohlfs, Wilson & Hüttemeister 2000, with $F_{\rm H\,I}$ in Jy km s^{-1}, $M_{\rm H\,I}$ in M$_\odot$, D in Mpc). The $S_{60\,\mu m}$ and $S_{100\,\mu m}$ FIR flux densities were combined in the usual manner to calculate the FIR luminosity ($L_{\rm FIR}$ in units of $L_{\rm FIR\odot}$) via $L_{\rm FIR} = 3.94 \times 10^5\,D^2(2.58\,S_{60\,\mu m} + S_{100\,\mu m})\,C$ (Solomon et al. 1997; column 9). Here, D is the distance in Mpc and C is a colour correction, which

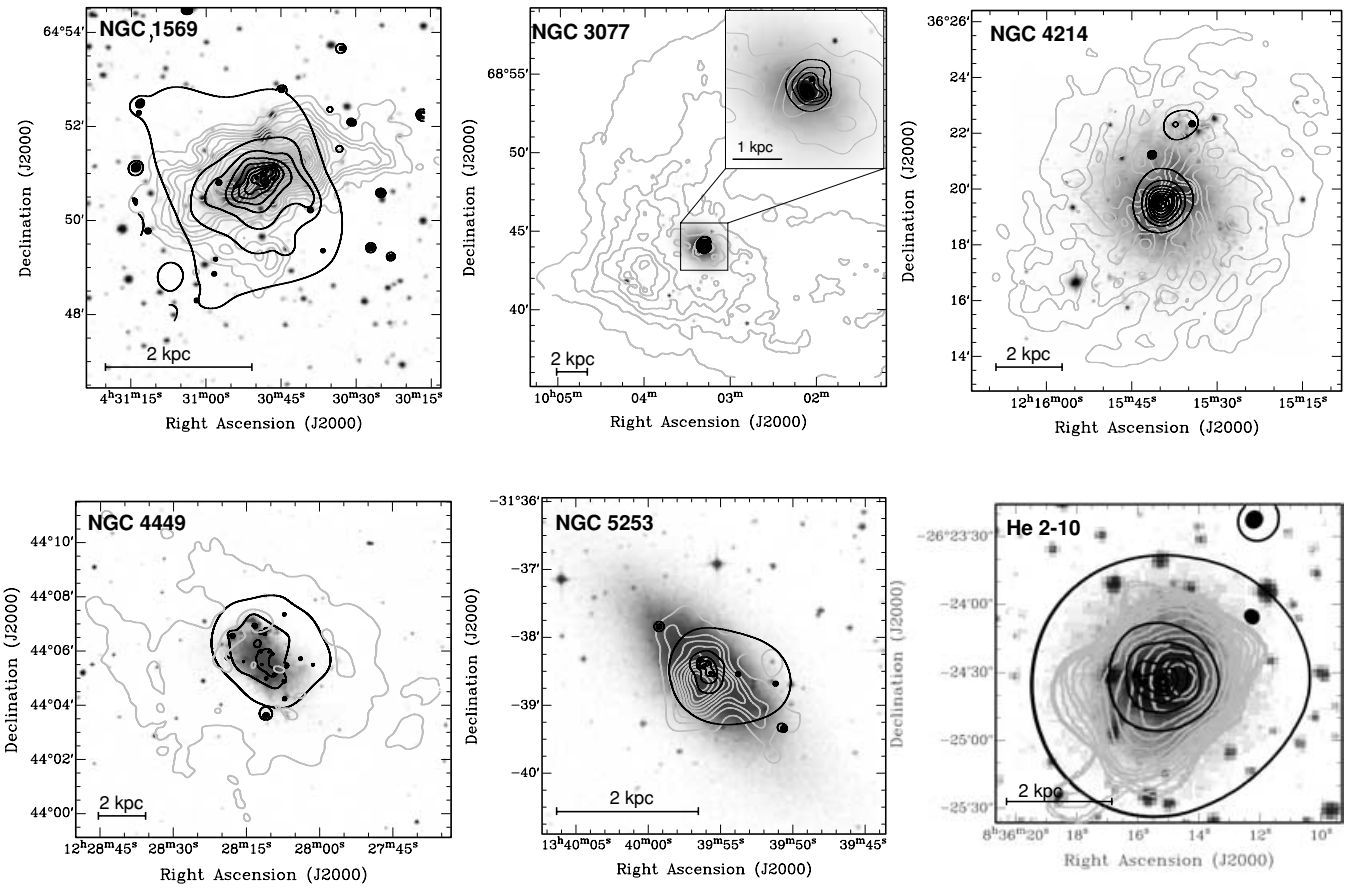

Figure 1. Optical images of dwarf galaxies with detections of diffuse X-rays. The black contours show the adaptively smoothed X-ray emission. Grey contours show H I emission; the contours start at 10^{20} cm^{-2} and are spaced by 5×10^{20} cm^{-2} for all but He 2–10 (images taken from Mühle 2003, Walter et al. 2002, Hunter et al. 1999 and Kobulnicky & Skillman 1995, respectively). Note the enlarged image in the upper right corner of the central region of NGC 3077. The H I contours of He 2–10 (taken from Kobulnicky et al. 1995) are not equally spaced; the outermost contour is at approximately 10^{20} cm^{-2}, which is 2 per cent of the peak intensity, and the innermost contour is at a level of 95 per cent [optical images taken from the Digital Sky Survey (NGC 1569), Walter et al. 2002 (NGC 3077, *R* band), Walter et al. 2001 (NGC 4214, *B* band), Frei et al. 1996 [NGC 4449, *R* band], Lauberts & Valentijn 1989 (NGC 5253, He 2–10, *R* band)].

depends on the $S_{60\,\mu m}/S_{100\,\mu m}$ ratio. The colour correction varies in the range of $1.5 < C < 2.1$ and, for simplicity, we adopted a common, mean colour correction of $C = 1.8$ for all galaxies. This range for C has been incorporated in the errors quoted for the fluxes. Using the conversion factor of Kennicutt (1998), we derive FIR SFRs, SFR_{FIR}, via $SFR_{FIR} = L_{FIR}/(5.8 \times 10^9\, L_{FIR,\odot})\ M_\odot\ yr^{-1}$ (column 10). Furthermore, masses of the cool dust (M_{dust} in units of $M_\odot$; column 11) were estimated from the FIR 60- and 100-μm flux densities (in Jy) by using the equation given in Huchtmeier, Sage & Henkel (1995): $M_{dust} = 4.78\, S_{100\,\mu m}\, D^2\{\exp[2.94(S_{100\,\mu m}/S_{60\,\mu m})^{0.4}] - 1\}$. This equation, however, was derived for a simple dust model assuming a single temperature of ∼40 K. As this needs not to be the case for the galaxies in our sample, we generally adopt a higher uncertainty of 50 per cent. An estimate for the lifetimes of the starbursts ($t_{life} = M_{H\,I}/SFR_{H\alpha}$) is listed in column 12. Column 13 lists the gas-to-light $M_{H\,I}/L_B$ ratios.

3 THE X-RAY MORPHOLOGY OF THE STARBURST DWARF GALAXIES

Of the eight dwarf starburst galaxies, we detect diffuse X-ray emission in all but two objects (detected in NGC 1569, NGC 3077, NGC 4214, NGC 4449, NGC 5253 and He 2–10), which can be attributed to hot, coronal gas stored in galactic winds (Paper I). The development of such a wind is expected to depend on the morphology of the cooler and denser gas within its host galaxy. In Fig. 1, a comparison of the optical, H I and X-ray morphologies is made. The first H I column density contour corresponds to 10^{20} cm^{-2} and the outermost X-ray contour is at approximately the 3–4σ detection limit. The X-ray emission of NGC 1569 extends well beyond its optical and H I counterparts perpendicular to the disc. The situation is different for the other five galaxies: the X-ray, Hα (see Fig. 2) and H I emission of He 2–10 are all fairly circularly shaped and have approximately the same size. Hot gas is almost entirely bound to the central region of NGC 4214 (note that the X-ray emission to the north has low significance and might be an artefact from the adaptive smoothing process). The optical and X-ray emission of NGC 3077 and 4449 is surrounded by an extended H I envelope, which can be ascribed to tidal debris resulting from a current interaction (see, e.g. Yun, Ho & Lo 1994; Hunter et al. 1998). The H I and X-ray emission of NGC 5253 have approximately the same size and both are embedded within a larger optical counterpart. Judging from these two-dimensional images, the hot gas in NGC 3077, 4214 and 4449 is still contained by the cooler, neutral medium. It might be expanding more freely in NGC 1569, NGC 5253 and He 2–10. The influence of the neutral ISM might also be obvious from the asymmetric shape of the hot outflows, which is apparent for all galaxies but He 2–10 and NGC 4214. In detail, NGC 1569 shows outflow

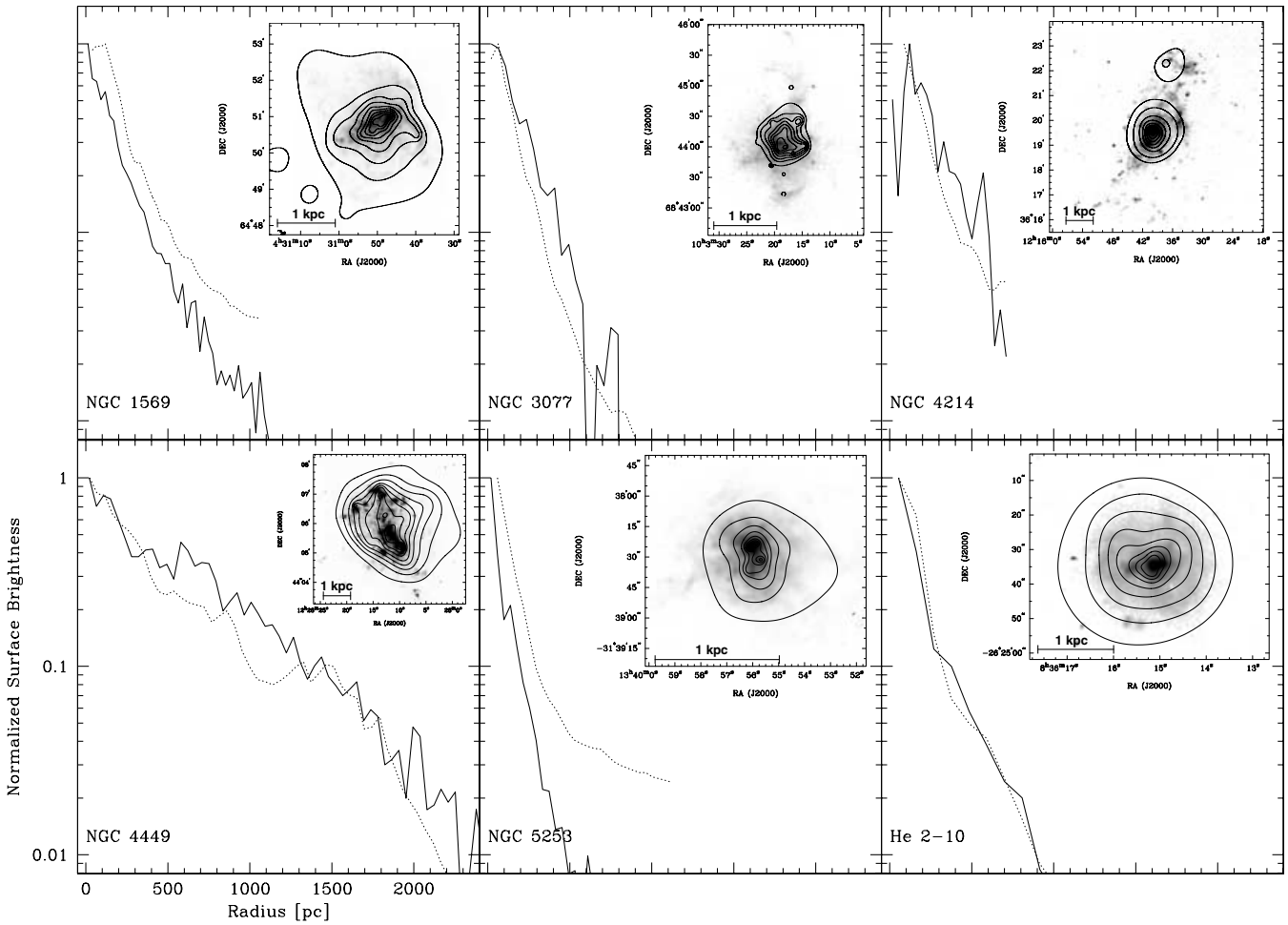

Figure 2. Azimuthally averaged Hα (dotted lines; excluding bright compact H II regions) and X-ray (solid lines) surface brightness profiles. All profiles are normalized to their maximum value and are on the same scale. Note the strong correlation between the X-ray and Hα profiles. The inserts are overlays of adaptively smoothed diffuse X-ray emission on the Hα images (all logarithmically scaled; see Paper I for details).

features towards the northern and southern direction. In addition, some of its hot gas seems to accumulate in a region that is half way between the gaseous disc and its fainter, southern extension. The well-known arm toward a westerly direction of NGC 1569 is visible in optical, Hα and X-ray images (see Fig. 2 and Paper I). The X-ray emission of NGC 3077 is more extended towards the north than towards the south (see also Fig. 2 and Ott, Martin & Walter 2003, hereafter OMW03). Finally, NGC 4449 and 5253 show an extension in X-rays towards a westerly direction. The hot gas seems always to be elongated along a direction that corresponds to that of least resistance, along the steepest gradient in H I, as can be expected from the hydrodynamics of a hot, tenuous plasma that interacts with a neutral, denser environment. In absolute terms, the H I gradients of NGC 1569, NGC 5253 and He 2–10 are much steeper than the extended H I envelopes of NGC 3077, 4449 and 4214. Note, however, that this analysis is based on the two-dimensional morphologies. In fact, an extension of the hot gas along the line of sight is more than likely but difficult to determine along with the three-dimensional morphology of the H I component.

In Fig. 2, we compare the Hα and diffuse X-ray morphologies directly by overlaying the corresponding maps. In the same figure, we also compare azimuthally averaged surface brightness profiles, which have been normalized to their peak intensities. Bright compact H II regions are excluded for this analysis. In general, the two different profiles are very similar, which is also obvious from the scalelengths of the two profiles listed in Table 4. Martin (1997) shows that while photoionization is the main process for Hα emission in the disc of starburst galaxies, the emission emerging from the halo is mainly a result of shocks (see Section 1). Leaking photons from H II regions, forward shocks emitting Hα radiation and reverse shocks that thermalize the hot gas to X-ray emitting temperatures are all the result of the impact of massive stars on the ISM. Because the starbursts are not as much confined to the nuclei of the galaxies as, for example, in the massive starburst galaxies M 82 and NGC 253, this may explain the similarity of the Hα and X-ray surface brightness profiles on global scales in the starburst galaxies

Table 4. Scalelengths (in pc) of exponential functions fitted to azimuthally averaged X-ray [total band, $h_{\rm X(Total)}$] and Hα surface brightness profiles ($h_{\rm H\alpha}$).

Galaxy	$h_{\rm X(Total)}$	$h_{\rm H\alpha}$
NGC 1569	208 ± 6	185 ± 8
NGC 3077	186 ± 10	140 ± 4
NGC 4214	145 ± 12	127 ± 3
NGC 4449	579 ± 15	524 ± 19
NGC 5253	109 ± 9	109 ± 3
He2-10	186 ± 15	227 ± 9

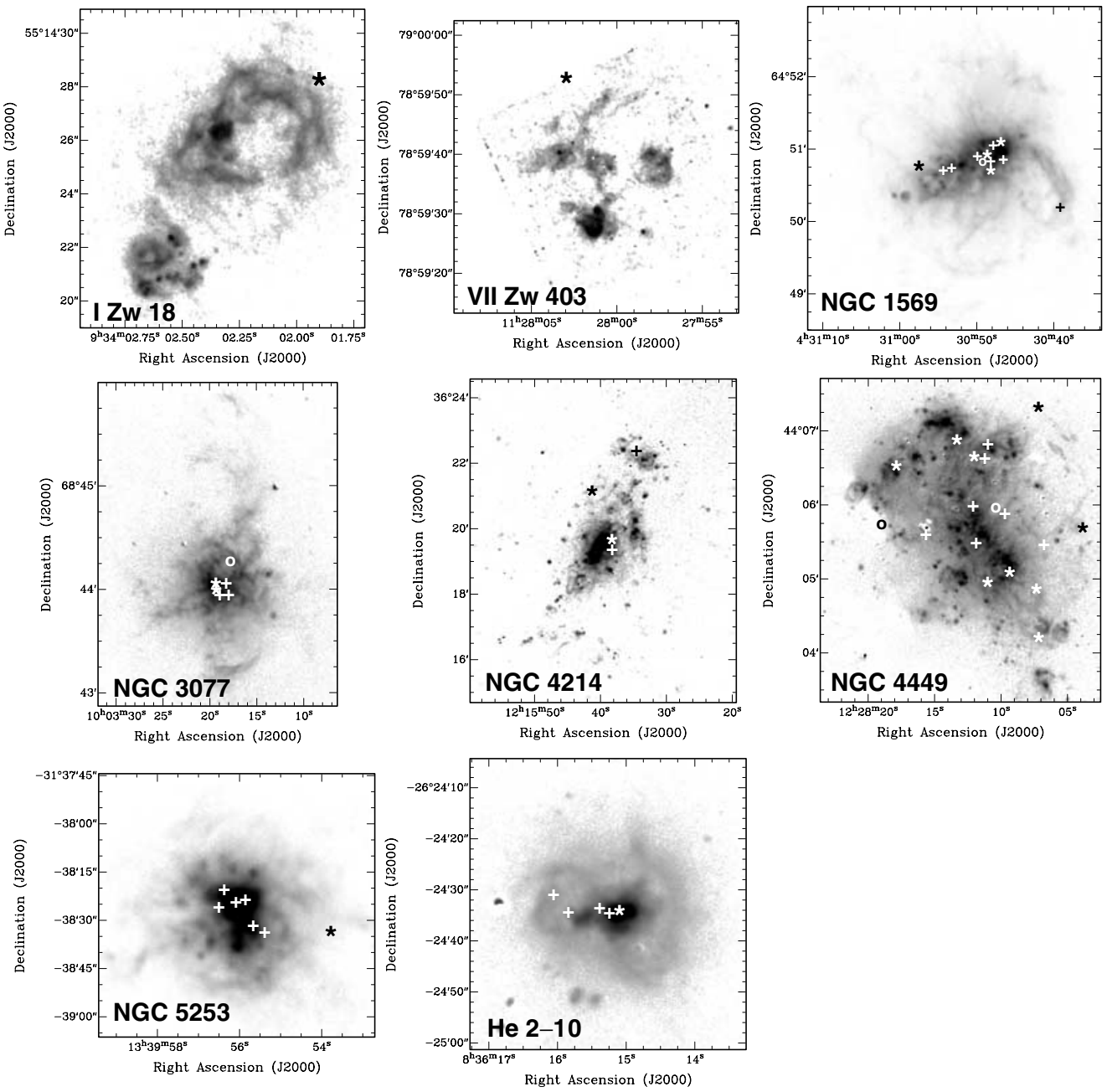

Figure 3. Hα images of the galaxies in the sample (logarithmic scale). The location of X-ray point sources are overplotted and marked according to their spectral type: star, power law (PL); cross, thermal plasma (TP); and circle, blackbody (BB) spectrum.

(see also Section 6). As a result of the different locations of the forward and reverse shocks, however, the hot gas and the Hα emission do not trace each other exactly on local scales, e.g. the expanding Hα shells in NGC 3077 are filled with hot gas (see OMW03), and the prominent Hα arm in NGC 1569 is somewhat displaced from a similar feature seen in X-rays (see Fig. 2 and Martin, Kobulnicky & Heckman 2002).

4 X-RAY POINT-SOURCE POPULATIONS

4.1 Distribution of X-ray point sources

X-ray point sources in the galaxy sample are detected mainly close to the centres of the galaxies. The only exception is NGC 4449 where the sources are more uniformly scattered across the entire optical body (see Fig. 3). The reason might be that NGC 4449 has a different SF history as compared with the other galaxies. This is exemplified by the Hα emission in NGC 4449, which is more uniformly distributed over its optical body, whereas again the other galaxies in the sample show a more concentrated surface brightness (Fig. 2; see also the Hα and X-ray scalelengths, which are for NGC 4449 a factor of 2.5 larger than for any other galaxy, Table 4).

In general, the brightest population of extragalactic X-ray point sources are active galactic nuclei (AGNs), X-ray binaries (XRBs), supernova remnants (SNRs) and supersoft sources. Except for AGNs, all of these sources need massive (progenitor) stars for their X-ray emission. For this reason, they are expected to concentrate

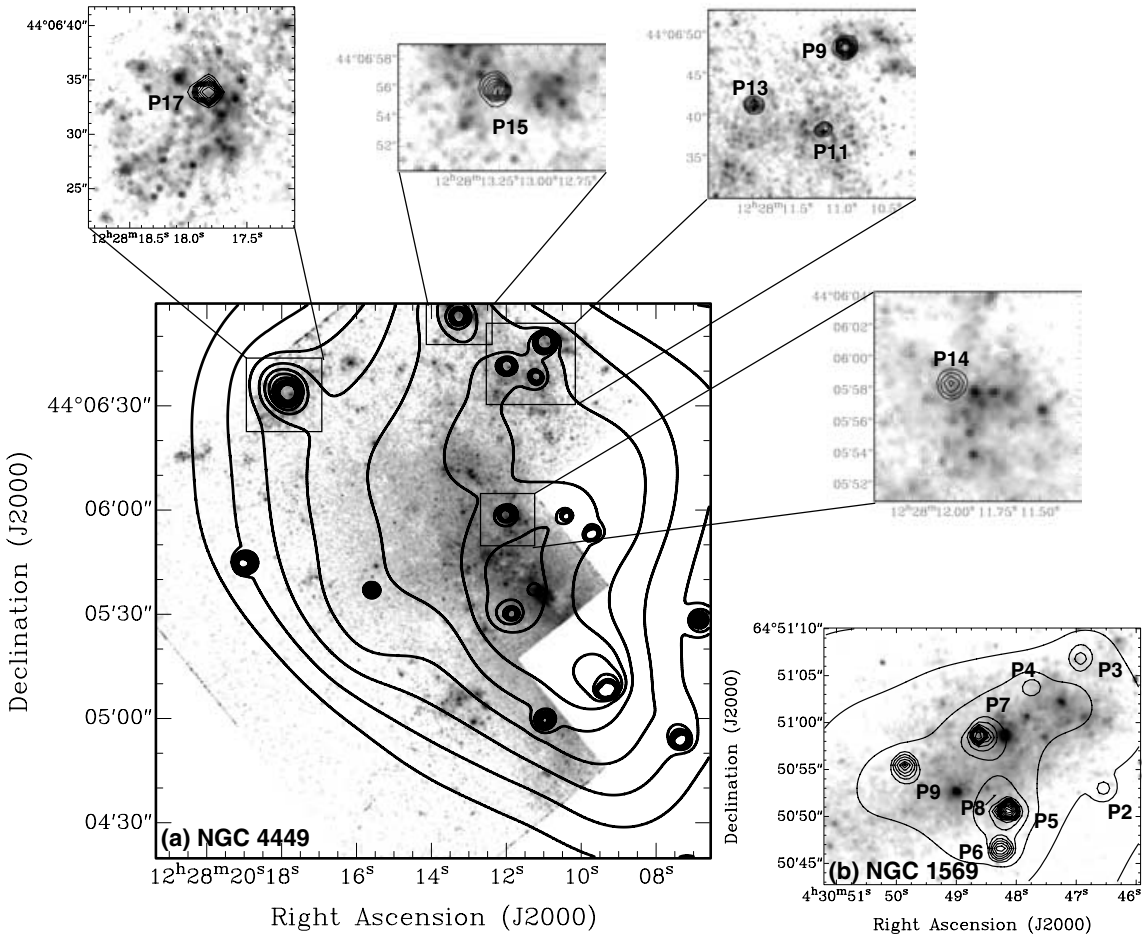

Figure 4. *Hubble Space Telescope* (*HST*)/Wide Field Planetary Camera 2 (WFPC2) images of NGC 4449 (a) and NGC 1569 (b) in the F336W (Johnson *U* band). Overlaid are contours of the *Chandra* X-ray observations. In some areas, X-ray point sources are close to bright young stellar clusters. In the case of NGC 4449, these regions are shown as enlarged images of the larger figure.

near star-forming regions or young stellar clusters. In Fig. 3, we overlay the location of the X-ray point sources on the Hα emission and indicate the type of model that best fits their spectra. The bulk of the point sources are detected in the vicinity of bright H II regions or on the rims of supergiant shells. Only a few sources cannot be related to individual Hα features. There is no obvious trend for a source type with galactocentric distance (see Paper I for details). Note that a certain fraction of point sources might also be unrelated foreground or background sources that are simply projected along the same line of sight as the galaxies under consideration.

Young, massive stars are very bright at ultraviolet (UV) wavelengths. Consequently, if X-ray point sources are related to star-forming regions, they should be spatially correlated with UV bright stellar clusters (note, however, that variable internal extinction can make a correlation more uncertain). F336W (corresponding to Johnson *U* band) images were available in the *Hubble Space Telescope* (*HST*)/Wide Field Planetary Camera 2 (WFPC2) archive for NGC 4449 and 1569 and, in Fig. 4, we show X-ray contours with labelled point sources overlaid on these images (for the labelling of the sources see Paper I). Almost all of the central X-ray point sources in NGC 1569 and most of the point sources in NGC 4449 that are covered by the WFPC2 field of view are located very close to UV bright stellar clusters but often slightly displaced. Those sources are likely associated with recent SF events. There is no relation, though, between the location of these sources and the shape of their X-ray spectrum, be it represented by power-law (PL), thermal plasma (TP), or blackbody (BB) shapes (see also Fig. 3 and Paper I). This is in conflict with the models by Kaaret et al. (2004), which imply that the slightly displaced sources are all XRBs.

4.2 X-ray point sources as a measure for star formation

The proximity of the X-ray sources and the H II regions/young stellar clusters suggests that the number of X-ray point sources might be a tracer for SF in general. Such a correlation was suggested by Grimm, Gilfanov & Sunyaev (2003) for high-mass XRBs. In Fig. 5, we plot the number of X-ray point sources as a function of different SF tracers: the Hα , the FIR and the blue (*B* band) luminosity. Trends are apparent for all three SF tracers. The correlation is best for the FIR luminosity and the blue luminosity. There is a larger scatter in the case of the Hα luminosities. Least-square fits to the data result in the following equations (n: number of X-ray point sources): $SFR_{\rm H\alpha}/({\rm M}_\odot\,{\rm yr}^{-1}) = (0.025 \pm 0.008)\,n$, $SFR_{\rm FIR}/({\rm M}_\odot\,{\rm yr}^{-1}) = (0.022 \pm 0.013)\,n$ and $L_{\rm B}/(10^8\,{\rm L}_B\odot) = (2.45 \pm 0.27)\,n$. He 2–10 is approximately 3 times more distant than the majority of the sample. Therefore, the detection limit is higher and point sources with a low X-ray flux will fall below this limit

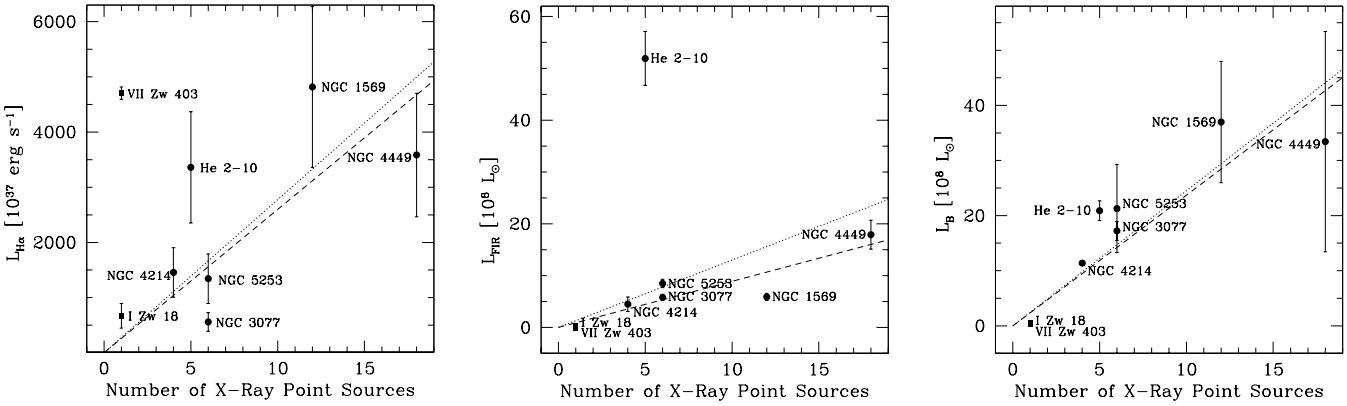

Figure 5. Star formation (SF) tracers Hα , far-infrared (FIR) and blue luminosity plotted against the number of X-ray point sources. Fits including (excluding) He 2–10 are displayed by dashed (dotted) lines.

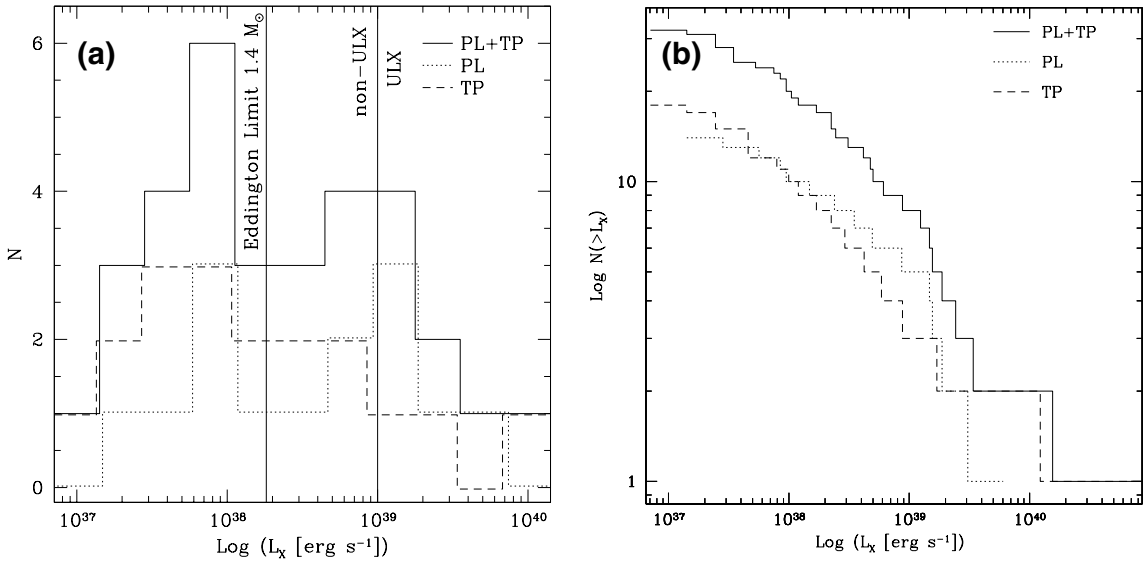

Figure 6. (a) Differential luminosity function of the X-ray point sources within all galaxies in the sample best fitted by a MeKaL thermal plasma (TP) or power-law (PL) spectrum as well as the combination of these two functions. N is the number of point sources and $L_{\rm X}$ the X-ray luminosity. The left vertical line displays the Eddington limit for a 1.4 $M_\odot$ source and the right vertical line marks the threshold for ultraluminous X-ray sources (ULXs). (b) Cumulative version of (a).

(for detection limits, see Paper I). For this reason, we fitted the same relations excluding this galaxy, which yields $SFR_{\rm H\alpha}/({\rm M}_\odot\,{\rm yr}^{-1}) = (0.023 \pm 0.008)\,n$, $SFR_{\rm FIR}/({\rm M}_\odot\,{\rm yr}^{-1}) = (0.015 \pm 0.002)\,n$ and $L_{\rm B}/(10^8\,{\rm L}_B\odot) = (2.37 \pm 0.26)\,n$. These relations suggest that the starburst is responsible not only for the hot gas but also for the X-ray point sources (see also Fig. 10).

4.3 Point-source luminosity function

A differential as well as a cumulative luminosity function of all the point sources in the galaxies is shown in Fig. 6. In this plot, we mark the location of the Eddington luminosity limit of a 1.4 $M_\odot$ star (a star at the Chandrasekhar limit), i.e. the X-ray luminosity at which the photon pressure equals the gravitational pull of the receptor star. In addition, we plot the luminosity limit for ultraluminous X-ray sources (ULXs, definition: $L_{\rm X} > 10^{39}$ erg s^{-1}), which in fact is the Eddington luminosity of a $\sim$7.7 $M_\odot$ object, a mass that is often used as a lower limit for SNe progenitor stars (e.g. Leitherer et al. 1999). Approximately 10 X-ray point sources in our sample can be classified as ULXs. These sources, intermediate-mass black holes or high-mass XRBs with accretion above the Eddington limit (for a discussion of ULXs, see, e.g. King 2004), are only found in I Zw 18 (one source), NGC 4449 (five, including two that are best fitted by BB spectra) and He 2–10 (four). These figures are even larger than the average number of ULXs in massive but non-starburst galaxies ($\sim$2, see Colbert & Ptak 2002). In merging galaxies such as the Antennae, however, the number of ULXs appears to be substantially increased (Zezas & Fabbiano 2002). Indeed, I Zw 18 and NGC 4449 are clearly interacting galaxies (Hunter et al. 1998; van Zee et al. 1998; Theis & Kohle 2001) and for He 2–10 a merger scenario has been proposed in the literature (Conti & Vacca 1994; Kobulnicky et al. 1995). However, NGC 3077 is also interacting but does not have any ULXs. On the basis of our limited sample, it is not possible to derive any clear dependence

Table 5. Results of fits of collisional thermal plasma (TP) models to the X-ray spectra applied to the entire galaxy, the centre and outer regions. This table is a shortened version of the corresponding tables in Paper I (fluxes and luminosities are given within an energy range of 0.3–8.0 keV).

Region	$N_{\rm H}$ (10^{21} cm^{-2})	T (10^6 K)	*Norm*[a] (10^{-5})	$F_{\rm X}^{\rm abs}$ (10^{-15} erg s^{-1} cm^{-2})	$F_{\rm X}$ (10^{-15} erg s^{-1} cm^{-2})	$L_{\rm X}$ (10^{37} erg s^{-1})	$\chi^2_{\rm red}$
				NGC 1569			
Total	$2.86^{+0.15}_{-0.15}$	$7.23^{+0.12}_{-0.12}$	$80.0^{+1.5}_{-1.5}$	205^{+10}_{-10}	721^{+15}_{-15}	$41.7^{+6.0}_{-6.0}$	0.98
Centre	$4.99^{+0.19}_{-0.19}$	$7.23^{+0.13}_{-0.13}$	$55.2^{+1.2}_{-1.2}$	116^{+7}_{-7}	497^{+13}_{-13}	$28.8^{+4.1}_{-4.1}$	0.68
Outer regions	$9.12^{+0.27}_{-0.26}$	$3.51^{+0.06}_{-0.06}$	125^{+5}_{-4}	$58.8^{+6.2}_{-5.8}$	809^{+36}_{-36}	$46.8^{+6.9}_{-6.9}$	0.78
				NGC 3077			
Total	$4.71^{+0.11}_{-0.11}$	$2.32^{+0.04}_{-0.04}$	$50.7^{+2.8}_{-2.8}$	$33.6^{+5.6}_{-5.1}$	1062^{+71}_{-69}	165^{+26}_{-26}	0.43
Centre	$0.86^{+0.32}_{-0.28}$	$6.04^{+0.72}_{-0.87}$	$0.39^{+0.05}_{-0.05}$	$6.16^{+1.95}_{-1.85}$	$11.2^{+1.6}_{-1.8}$	$1.74^{+0.37}_{-0.37}$	0.11
Outer regions	$4.52^{+0.14}_{-0.13}$	$2.30^{+0.04}_{-0.04}$	$30.5^{+2.2}_{-2.2}$	$21.6^{+4.7}_{-4.1}$	637^{+54}_{-53}	$98.7^{+16.3}_{-16.3}$	0.44
				NGC 4214			
Total	$9.87^{+0.59}_{-0.52}$	$2.17^{+0.06}_{-0.06}$	129^{+14}_{-14}	$37.9^{+12.9}_{-10.6}$	759^{+98}_{-95}	$75.9^{+14.5}_{-14.5}$	0.14
Centre	$10.1^{+1.4}_{-1.1}$	$2.80^{+0.27}_{-0.28}$	$22.7^{+5.3}_{-5.3}$	$12.5^{+9.8}_{-6.7}$	155^{+44}_{-41}	$15.5^{+4.9}_{-4.9}$	0.04
Outer regions	$2.91^{+0.67}_{-0.56}$	$2.68^{+0.21}_{-0.24}$	$12.2^{+1.8}_{-1.8}$	$25.8^{+11.3}_{-9.6}$	$82.3^{+14.9}_{-15.6}$	$8.23^{+1.95}_{-1.95}$	0.14
				NGC 4449			
Total	$7.19^{+0.10}_{-0.10}$	$2.98^{+0.03}_{-0.03}$	353^{+7}_{-7}	393^{+21}_{-20}	2481^{+55}_{-55}	452^{+65}_{-65}	1.07
Centre	$7.87^{+0.23}_{-0.22}$	$3.12^{+0.07}_{-0.07}$	71^{+3}_{-3}	$75.9^{+9.2}_{-8.5}$	510^{+26}_{-26}	$92.8^{+14.0}_{-14.0}$	0.26
Outer regions	$4.88^{+0.13}_{-0.12}$	$3.33^{+0.05}_{-0.05}$	111^{+3}_{-3}	225^{+15}_{-15}	821^{+26}_{-25}	149^{+22}_{-22}	0.83
				NGC 5253			
Total	$5.67^{+0.23}_{-0.22}$	$3.51^{+0.08}_{-0.08}$	$55.5^{+2.0}_{-2.1}$	$81.6^{+8.6}_{-8.1}$	359^{+18}_{-17}	$46.6^{+7.0}_{-7.0}$	0.64
Centre	$10.1^{+0.3}_{-0.3}$	$3.79^{+0.09}_{-0.09}$	$44.6^{+2.0}_{-2.0}$	$39.3^{+5.0}_{-4.6}$	299^{+17}_{-17}	$38.9^{+5.9}_{-5.9}$	0.23
Outer regions	$7.58^{+0.88}_{-0.75}$	$3.21^{+0.23}_{-0.19}$	$25.6^{+3.4}_{-3.4}$	$24.6^{+10.1}_{-7.8}$	158^{+27}_{-25}	$20.6^{+4.6}_{-4.6}$	0.49
				He 2-10			
Total	$4.44^{+0.35}_{-0.29}$	$2.82^{+0.14}_{-0.14}$	$93.6^{+13.0}_{-13.0}$	103^{+46}_{-36}	2101^{+319}_{-313}	2038^{+423}_{-423}	0.32
Centre	$1.23^{+0.22}_{-0.20}$	$7.60^{+0.44}_{-0.44}$	$3.38^{+0.27}_{-0.27}$	$41.9^{+6.9}_{-6.5}$	$95.6^{+6.3}_{-6.4}$	$92.7^{+14.5}_{-14.5}$	0.09
Outer regions	$2.82^{+0.15}_{-0.14}$	$3.21^{+0.11}_{-0.10}$	$17.5^{+1.2}_{-1.2}$	$50.4^{+9.9}_{-9.1}$	410^{+32}_{-31}	397^{+64}_{-64}	0.22

[a]The normalization is given by $10^{-14}(4\pi D^2)^{-1}\int n_{\rm e} n_{\rm H} {\rm d}V$ with: D, the distance in cm; $n_{\rm e}$, $n_{\rm H}$, the electron and proton densities in cm^{-3}; and V, the volume in cm^3.

between the strength of the galaxy interaction and the number of ULXs.

A PL fit to the cumulative luminosity distribution for all sources results in a slope of $\alpha = 0.24 \pm 0.06$ [$N(>L_{\rm X}) \propto L_{\rm X}^{-\alpha}$]. This value has been derived using the data of the differential luminosity distribution following the method described in Crawford, Jauncey & Murdoch (1970). As a result of our completeness limits, data bins with luminosities less than 10^{38} erg s^{-1} were discarded for this fit. Similar fits for the individual PL and TP source populations lead to very similar slopes of $\alpha = 0.23 \pm 0.08$ (PL) and 0.25 ± 0.08 (TP). The PL index derived here for the dwarf starburst galaxies is shallower than those observed in more massive starbursts such as NGC 253, M 82 and the Antennae (indices of ∼0.4–0.8). The PL indices of non-starburst galaxies ($\alpha \sim 1.2$) are far steeper than both, the value for our sample and the PL indices of more massive starburst galaxies (for a comparison of starburst and non-starburst cumulative luminosity functions see Kilgard et al. 2002).

5 X-RAY PROPERTIES OF THE HOT CORONAL GAS

In Paper I, we performed one-temperature MeKaL thermal equilibrium plasma fits (Mewe, Gronenschild & van den Oord 1985; Kaastra 1992; Liedahl, Osterheld & Goldstein 1995), to the diffuse X-ray emission within certain regions of the galaxies. In addition to fitting the total emission resulting from diffuse gas, we also made fits to the emission from the centre and various regions around it. Table 5 shows the main fitting results listing the absorbing column densities $N_{\rm H}$, the temperature T, the normalization, absorbed X-ray flux $F_{\rm X}^{\rm abs}$, unabsorbed X-ray flux $F_{\rm X}$ and unabsorbed X-ray luminosity $L_{\rm X}$. The fits are used to determine intrinsic parameters of the hot gas: the electron volume density $n_{\rm e}$ follows from the normalization of the spectra assuming a spherical geometry, and that the proton and electron density are the same over the volume V (see OMW03); other parameters that can be derived are the equivalent diameter $d_{\rm eq}$ of the X-ray emitting region ($d_{\rm eq} = \sqrt{4Area/\pi}$, where *Area* is the area of the emission), the mean line of sight l, the emission measure $EM = n_{\rm e}^2 l$, the pressure of the hot gas $P/k = 2\,n_{\rm e}\,T$ (k: Boltzmann's constant), its mass $M_{\rm hot} = n_{\rm e} m_{\rm p} V$ ($m_{\rm p}$, proton mass; V, shell volume), the thermal energy $E_{\rm th} = 3 n_{\rm e} VkT$, the cooling time $t_{\rm cool} = E_{\rm th}/L_{\rm X}$, the mass deposition rate $\dot{M}_{\rm cool} = M_{\rm hot}/t_{\rm cool}$ and finally the mean thermal velocity per particle $\langle v_{\rm hot}\rangle = \sqrt{2E_{\rm th}/M_{\rm hot}}$. The quantities for the different galaxies are listed in Table 6. Note that most of these values depend on the volume filling factor $f_{\rm v}$ and the metallicity Z. For the metallicities, we use those derived for H II regions in the individual objects (for a discussion see Paper I). As $f_{\rm v}$ is a priori unknown, we derive all gas parameters for $f_{\rm v} = 1$, any corrections for lower filling factors must be applied according to the table header in Table 6. High angular resolution *Chandra*

Table 6. Derived parameters of the hot gas. All values were determined for a filling factor $f_{\rm v} = 1$ and metallicities $Z_{\rm H\,II}$ as derived for the H II regions in the objects (see Table 3). The values can be converted to lower filling factors and other metallicities Z (via $\xi = Z/Z_{\rm H\,II}$) of the X-ray emitting gas as given in the head of the table.

Region	$d_{\rm eq}$ (pc)	l (pc)	$n_{\rm e}$ $[\times(f_{\rm v}\xi)^{-0.5}]$ $(10^{-3}\,{\rm cm}^{-3})$	EM $[\times(f_{\rm v}\xi)^{-1}]$ $({\rm cm}^{-6}\,{\rm pc})$	P/k $[\times(f_{\rm v}\xi)^{-0.5}]$ $(10^5\,{\rm K\,cm}^{-3})$
			NGC 1569		
Total	2100 ± 210	1400 ± 140	18 ± 2	0.45 ± 0.05	2.61 ± 0.27
Centre	820 ± 82	540 ± 54	61 ± 6	2.03 ± 0.20	8.87 ± 0.91
Outer regions	1580 ± 158	1060 ± 106	35 ± 4	1.26 ± 0.13	2.42 ± 0.25
			NGC 3077		
Total	1820 ± 182	850 ± 85	29 ± 3	0.72 ± 0.07	1.35 ± 0.14
Centre	300 ± 30	200 ± 20	38 ± 5	0.29 ± 0.03	4.61 ± 0.86
Outer regions	1360 ± 136	900 ± 90	35 ± 4	1.10 ± 0.11	1.61 ± 0.17
	NGC 4214				
Total	1270 ± 127	850 ± 85	64 ± 7	3.50 ± 0.35	2.78 ± 0.33
Centre	410 ± 41	270 ± 27	147 ± 23	5.81 ± 0.58	8.21 ± 1.51
Outer regions	910 ± 91	600 ± 60	33 ± 4	0.63 ± 0.06	1.74 ± 0.27
			NGC 4449		
Total	4120 ± 412	2740 ± 274	24 ± 2	1.63 ± 0.16	1.46 ± 0.15
Centre	1000 ± 100	660 ± 66	92 ± 9	5.54 ± 0.55	5.71 ± 0.60
Outer regions	2820 ± 282	1880 ± 188	24 ± 2	1.10 ± 0.11	1.61 ± 0.16
			NGC 5253		
Total	2340 ± 234	1560 ± 156	19 ± 2	0.57 ± 0.06	1.34 ± 0.14
Centre	840 ± 84	560 ± 56	80 ± 8	3.56 ± 0.36	6.05 ± 0.64
Outer regions	1740 ± 174	1160 ± 116	20 ± 2	0.48 ± 0.05	1.30 ± 0.18
			He 2–10		
Total	3180 ± 318	2120 ± 212	43 ± 5	3.88 ± 0.39	2.41 ± 0.32
Centre	500 ± 50	340 ± 34	130 ± 14	5.78 ± 0.58	19.83 ± 2.42
Outer regions	1960 ± 196	1300 ± 130	38 ± 4	1.90 ± 0.19	2.45 ± 0.27

Region	$M_{\rm hot}$ $[\times f_{\rm v}^{0.5}\xi^{-0.5}]$ $(10^4\,{\rm M}_\odot)$	$E_{\rm th}$ $[\times f_{\rm v}^{0.5}\xi^{-0.5}]$ $(10^{52}\,{\rm erg})$	$t_{\rm cool}$ $[\times f_{\rm v}^{0.5}\xi^{-0.5}]$ (Myr)	$\dot{M}_{\rm cool}$ $(10^{-3}\,{\rm M}_\odot\ {\rm yr}^{-1})$	$<v_{\rm hot}>$ $({\rm km\,s}^{-1})$
			NGC 1569		
Total	216 ± 68	772 ± 244	586 ± 204	3.69 ± 1.74	599 ± 134
Centre	44 ± 14	156 ± 50	172 ± 60	2.55 ± 1.20	599 ± 134
Outer regions	176 ± 56	306 ± 97	207 ± 72	8.54 ± 4.03	417 ± 94
			NGC 3077		
Total	227 ± 72	260 ± 83	50 ± 18	45.56 ± 21.67	339 ± 76
Centre	1.3 ± 0.4	4 ± 1	72 ± 30	0.18 ± 0.10	547 ± 131
Outer regions	114 ± 36	129 ± 41	41 ± 15	27.49 ± 13.19	338 ± 76
			NGC 4214		
Total	170 ± 55	182 ± 59	76 ± 28	22.40 ± 11.05	328 ± 75
Centre	13 ± 4	18 ± 6	37 ± 18	3.55 ± 2.06	373 ± 91
Outer regions	32 ± 10	42 ± 14	162 ± 66	1.97 ± 1.03	365 ± 85
			NGC 4449		
Total	2214 ± 700	3255 ± 1030	228 ± 79	97.16 ± 45.65	384 ± 86
Centre	119 ± 38	183 ± 58	62 ± 22	19.05 ± 9.02	393 ± 88
Outer regions	703 ± 223	1155 ± 366	245 ± 86	28.66 ± 13.50	406 ± 91
			NGC 5253		
Total	318 ± 101	551 ± 175	374 ± 131	8.50 ± 4.02	417 ± 94
Centre	61 ± 19	115 ± 36	93 ± 33	6.57 ± 3.12	433 ± 97
Outer regions	138 ± 45	219 ± 73	337 ± 135	4.11 ± 2.11	399 ± 92
			He 2–10		
Total	1784 ± 578	2482 ± 813	39 ± 15	463 ± 234	374 ± 86
Centre	21 ± 7	79 ± 26	27 ± 10	7.81 ± 3.76	614 ± 139
Outer regions	373 ± 119	591 ± 189	47 ± 17	79.22 ± 37.96	399 ± 90

observations of more massive starburst galaxies (see, e.g. Heckman 2002, and references therein) and hydrodynamical simulations (e.g. Strickland & Stevens 2000) reveal that the volume filling factor falls most likely in the range of 0.1–0.3 for superwinds. Confined shells, however, such as those in NGC 3077 (see OMW03) may have larger filling factors. An observational determination of the filling factor for dwarf galaxies is not an easy task as a result of their lower flux and the unknown source geometries. In addition, hydrodynamical simulations show that the filling factor can take up very different values. For the rest of this paper, we assume that f_v is approximately the same for all objects and that therefore the values may be compared, at least in a relative sense.

5.1 Non-detections

No diffuse X-ray emission is detected in I Zw 18 and VII Zw 403. The integration times of both objects are the lowest of all the galaxies in the sample and the detection limits of the unabsorbed luminosities are of order $\sim$2–4 $\times$ 10^{38} erg s^{-1} (see Paper I). This is approximately 1 order of magnitude lower than what is measured for the faintest galaxy with detection (Table 5). The 5–10 times smaller size of I Zw 18 and VII Zw 403 (see Table 1), however, reduces the volume of these galaxies up to 3 orders of magnitude. For this reason, the hot gas might be below the detection threshold if it has similar properties to that found in the rest of the sample. A second factor may be the metallicity of the gas, which controls the X-ray emissivity (see, e.g. Sutherland & Dopita 1993). As shown in Paper I, the metallicities of the hot gas are in agreement with the metallicities derived directly from H II regions. As I Zw 18 and VII Zw 403 are the objects with the lowest metallicities in the sample, this might push their X-ray luminosity below the detection threshold. In particular, all galaxies where diffuse X-ray emission is detected exhibit oxygen abundances in excess of $12 + \log(\mathrm{O/H}) \gtrsim 8.1$ (see Fig. 7).

Alternatively, a higher absorbing column density or a very high temperature can result in a non-detection with hot gas still being present in large quantities (note that the fitted column densities for the other objects are 2–4 times higher as compared with 1.5 $\times$ 10^{21} cm^{-2}, which are adopted for the determination of the detection threshold). We also cannot exclude that hot gas in I Zw 18 and VII Zw 403 has not formed or that the hot gas might have blown out of the gravitational potential of VII Zw 403 (see Section 7). Alternatively, it might have cooled down sufficiently to escape detection. The ages of the expanding Hα shells are indeed higher in I Zw 18 and VII Zw 403 (10–17 Myr) as compared with the other galaxies (1–10 Myr), see (Martin 1998; Silich et al. 2002). Another possibility would be that the conditions for developing shock fronts are different (see the models in Strickland et al. 2002). Deeper X-ray observations are needed for a final assessment.

5.2 Luminosities

Hot gas is detected in NGC 1569, NGC 3077, NGC 4214, NGC 4449, NGC 5253 and He 2–10. Their X-ray luminosities cover approximately 2 orders of magnitude. The galaxies with the lowest diffuse X-ray luminosities are NGC 1569 ($L_X = 4.2 \times 10^{38}$ erg s^{-1}) and NGC 5253 (4.7 $\times$ 10^{38} erg s^{-1}; Table 5). As shown in Section 3, these are the galaxies where the X-ray emission extends spatially beyond an H I column density of 10^{20} cm^{-2}. As most of the X-rays are produced by shocked and thermalized material, it may be that there is no material in the halo for the stellar ejecta to be hit, which reduces the X-ray luminosity. In addition, those objects are the two galaxies with diffuse X-ray emission showing the lowest metallicities ($\sim$20 per cent solar, see Table 3). As the X-ray emissivity of a given amount of material is a nearly linear function of metallicity (Sutherland & Dopita 1993), this could also be the cause for the low luminosity in these two objects. The galaxies where the diffuse X-ray emission seems to be still confined to the extended H I envelope show luminosities of 7.6 $\times$ 10^{38} erg s^{-1} (NGC 4214) and 4.5 $\times$ 10^{39} erg s^{-1} (NGC 4449). These galaxies have a slightly larger metallicity of $\sim$25 per cent solar. In He 2–10, the X-ray emission extends approximately as far as the size of the H I at 10^{20} cm^{-2}. It is the galaxy with the highest X-ray luminosity (2.0 $\times$ 10^{40} erg s^{-1}) and metallicity (approximately solar). The only galaxy with an X-ray luminosity that does not fit into the trend with metallicity, shown in Fig. 7, is NGC 3077 with a metallicity of solar and a relatively low X-ray luminosity of 1.7 $\times$ 10^{39} erg s^{-1}.

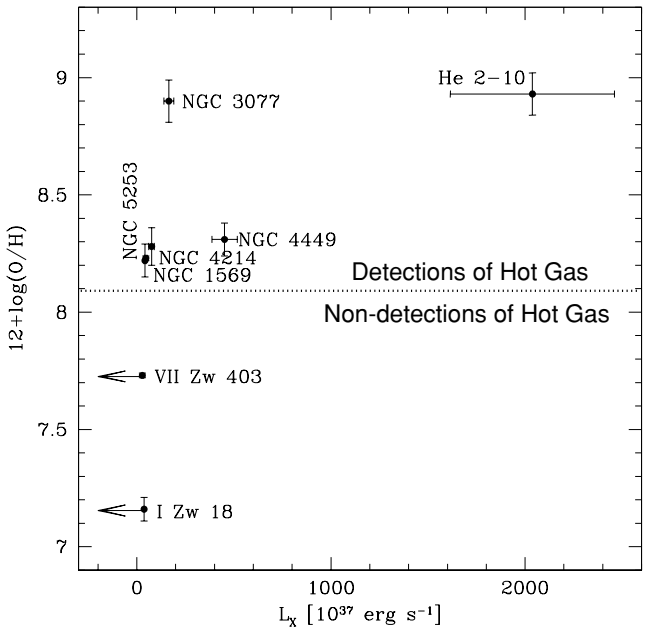

Figure 7. Oxygen abundance of H II regions plotted against the X-ray luminosity of the diffuse component. Below a threshold of $12 + \log(\mathrm{O/H}) \sim 8.1$ no hot gas is detected within the detection limits.

5.3 Temperatures

The temperature of the hot gas averaged over the total area is with $\sim$2.0–3.5 $\times$ 10^6 K approximately the same for all galaxies, except for NGC 1569 ($T \simeq 7.2 \times 10^6$ K). As described in Heckman, Lehnert & Armus (1993); Heckman (2002); Strickland et al. (2002), temperatures T in this range are the result of shocks and are a direct function of shock velocities v_s: $v_s = [(16/3)(kT/\mu)]^{0.5}$ (k, Boltzmann's constant; μ, mean mass per particle), resulting in $v_s \simeq 470$ km s^{-1} for $T = 3 \times 10^6$ K. This value is similar to the derived mean particle velocity of the hot, thermalized gas (Table 6). Except for NGC 4214, 4449 and 5253, the temperature of the hot gas stored in the outer regions of the galaxies is $\sim$2–3 times lower than in their centres (Table 5). As most of the X-rays emerge from shocked gas, this might be indicative of decelerating wind velocities, enhanced mass loading of cooler gas, or adiabatic cooling in the halo of the dwarf galaxies under study.

5.4 Absorbing column densities

The absorbing column densities that were fitted to the individual spectra are in the range of $\sim$3–7 $\times$ 10^{21} cm^{-2}. This is not in

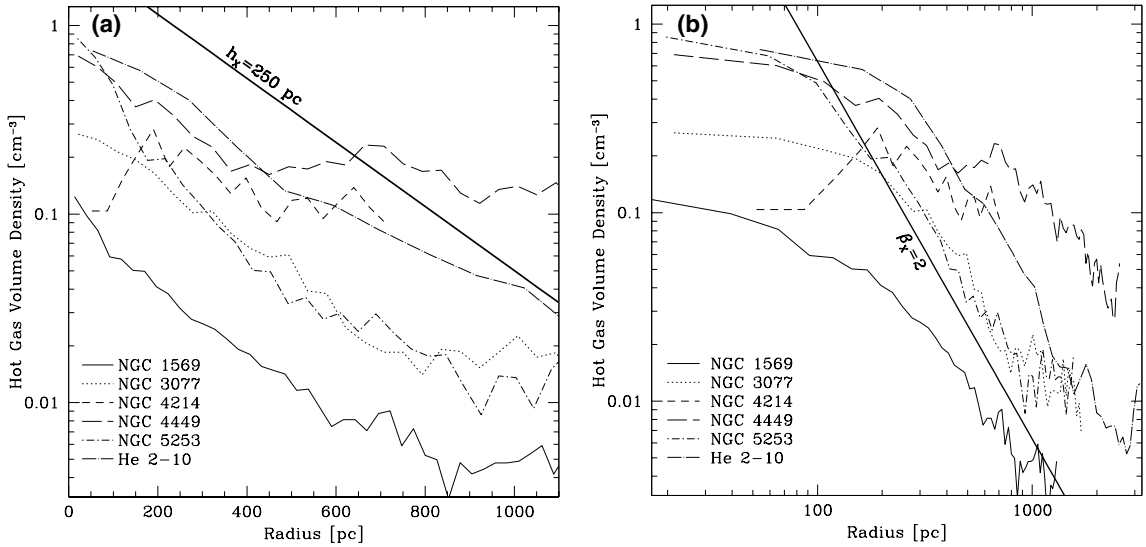

Figure 8. Azimuthally averaged volume density profile of the hot, X-ray emitting gas in logarithmic (a) and double logarithmic (b) units. For comparison, an exponential function with a scalelength of $h_X = 250$ pc and a power law (PL) with an index of $\beta_X = 2$ are displayed.

particularly good agreement with H I data. Observations of the 21-cm line of neutral hydrogen result in H I column densities of 0.1–2 $\times$ 10^{21} cm^{-2} (see Fig. 1). When the absorbing column density is fixed to the H I values, the fit to the X-ray spectra becomes worse in the soft regime. Also the application of non-equilibrium plasmas (XSPEC model XSNEI), a combination of two TP components, a TP with a PL (to incorporate some faint emission from unresolved point sources), or a variation of the α/Fe element abundance ratio does not lower the absorbing columns substantially, neither does fitting smaller regions (as done in Paper I) help.

A metallicity for the absorbing material that is higher than that of the H II regions can partly accommodate for this effect, but this is considered to be unlikely. An alternative explanation for the discrepancy of measured versus fitted H I column density might be that the gas is more clumpy, or that the contribution by molecular (and ionized gas) has been underestimated.

5.5 Volume densities

From the fits to the diffuse X-ray emission listed in Table 5, we derive that the mean volume densities of the hot gas are in the range of $n_e \simeq 0.02$–0.06 cm^{-3} averaged over each galaxy (Table 6). In general, volume densities at their centres are higher by a factor of $\sim$3 as compared with the outskirts. With the help of the X-ray surface brightness profiles (Fig. 2) and the method described in OMW03, we constructed volume density profiles assuming spherical geometries. Those profiles are shown in Fig. 8. In general, exponential fits are appropriate for the inner $\sim$400 pc, whereas PL models are better fits to the data at larger radii. Results of the fits are listed in Table 7. Except for NGC 4449, the exponential scalelengths of the volume densities are up to 50 per cent larger as compared with the azimuthally averaged X-ray surface brightness scalelengths (Table 4) and are in the range of 150–320 pc. The PL index β_X (definition: $n_e \propto r^{-\beta_X}$) for the outer parts of the profiles are all within a range of $\beta_X \sim 1.5$–2.0 with the only exception being NGC 4214 ($\beta_X = 0.81$, see Fig. 8). For comparison, a spherically-symmetric (and also a conical), freely flowing wind has a PL index of 2 (Chevalier & Clegg 1985), which is very close to the measured values (see also the discussion in Section 7).

Table 7. Scalelengths (h_X in pc) for exponential functions to the inner radii ($r \lesssim 350$–600 pc) of the volume density profiles and spectral indices for power-law (PL) fits (β_X) at larger radii.

Galaxy	h_X	β_X
NGC 1569	233 ± 7	1.72 ± 0.19
NGC 3077	274 ± 10	1.85 ± 0.14
NGC 4214	316 ± 67	0.81 ± 0.24
NGC 4449	272 ± 17	1.46 ± 0.07
NGC 5253	142 ± 7	1.85 ± 0.09
He 2–10	279 ± 38	1.96 ± 0.09

5.6 Pressures

The pressures of the hot gas are in the range of $P/k \simeq 1$–3×10^5 K cm^{-3} for all galaxies. The ISM in our Milky Way exhibits pressures of at most a few times 10^4 K cm^{-3} (see, e.g. Wolfire et al. 2003). If this value was also typical for dwarf galaxies undergoing a starburst, then the hot gas has an overpressure and will expand. This naturally explains the expanding Hα shells in the sample of galaxies under study (see, e.g. Marlowe et al. 1995; Martin 1996, 1998). The pressure of the hot gas has a gradient from the centre of the galaxies toward the outer regions (see Table 6); the pressures in the centres are on average $\sim$5 times higher than those in the outer regions. This is the result of the combined effect of both lower volume densities and lower temperatures in the outskirts.

5.7 Masses and mass loading of the hot gas

The masses of the hot gas (M_X) within the galaxies range from $\sim$2 to 20 $\times$ 10^6 M$_\odot$. Most of the mass is stored in the outer regions of the galaxies, which is a consequence of the much larger volume as compared with the centres. The mass of the hot gas is approximately 1 per cent of the H I content of the galaxies (see Tables 6 and 3).

We will now compare the mass injection from massive stars (M_{ej}) to M_X. For this purpose, we use the stellar evolution synthesis models published by Leitherer et al. (1999; STARBURST99).[1] In their

[1] http://www.stsci.edu/science/starburst99/

fig. 110, they show the mass loss of a stellar population undergoing a continuous starburst at a rate of $1\,M_\odot\,yr^{-1}$. Throughout this discussion, we will use the models based on a Salpeter initial mass function (IMF) with an upper mass cut-off of $100\,M_\odot$ and a lower mass cut-off of $1\,M_\odot$. As described in Martin (1998) and Méndez et al. (1999), expanding shells in most of the starburst galaxies in our sample have a kinematic age of $\sim 10^7$ yr. This expansion was mainly driven by the kinetic energy input of SNe, which explode $\sim 4 \times 10^7$ yr after the progenitor stars were created. For this reason, we evaluate the integrated mass loss at an age of 5×10^7 yr. At this age, the models are virtually independent of metallicity. To derive the final mass loss of the stellar population in the galaxies of our sample, we scale the STARBURST99 models at that point of stellar evolution by the current SFRs listed in Table 3 ($SFR_{H\alpha}$, based on Hα ; SFR_{FIR}, based on FIR measurements). The resulting M_{ej} is then used to compute the corresponding mass-loading factor χ_{ml}, which we define as

$$\chi_{ml} = \frac{M_X}{M_{ej}} - 1. \quad (1)$$

χ_{ml} therefore corresponds to the amount of entrained material relative to the mass of the stellar ejecta. The mass-loading factors χ_{ml} for our sample of galaxies are estimated to be: $-0.6/0.9$ (NGC 1569), $3.0/1.0$ (NGC 3077), $0.7/1.7$ (NGC 4214), $5.2/5.4$ (NGC 4449), $1.3/0.9$ (NGC 5253) and $4.3/0.8$ (He 2–10) where the first number is derived from $SFR_{H\alpha}$ and the second number using SFR_{FIR}. These estimates show that at least approximately the same amount as the stellar ejecta itself was entrained by the superwind. This material must have been shocked and/or boiled off the surrounding, cooler ISM (cf. the models of Weaver et al. 1977; Strickland et al. 2002). In the process, the hot gas was cooled down to the measured temperatures of a few times 10^6 K (see Table 5), which boosts the X-ray emissivity of the hot gas (see the cooling functions described in Sutherland & Dopita 1993). We note, however, that all of the above values were derived for a volume filling factor of unity and for a metallicity for each galaxy based on that of its H II regions. A lower filling factor, as suggested by the calculations of Strickland & Stevens (2000) or supersolar metallicities (e.g. as derived for NGC 1569 by Martin et al. 2002) will reduce the need for mass loading.

5.8 Thermal energies

The thermal energy (E_{th}) of the hot gas is a lower limit to the mechanical energy input of strong stellar winds and SNe. Only in the absence of cooling and under the condition of full thermalization both energies should be equal. E_{th} depends linearly on the mass of the hot gas and on its temperature. The temperatures of the galaxies in the sample are very similar (see Section 5.3). For this reason, the thermal energies vary, as do the masses, over an order of magnitude: $E_{th} \simeq 2\text{–}30 \times 10^{54}$ erg. Most of the thermal energy is stored in the outer regions rather than in the centres of the galaxies, which is the result of the much larger volume at larger radii. The total thermal energy corresponds to the kinetic energy output of ∼2000–30 000 SNe. This figure is confirmed by Hα spectroscopy of expanding shells (see Section 7). According to the STARBURST99 models, a stellar cluster with a combined mass of $10^6\,M_\odot$ releases an energy of $\sim 10^{55}$ erg (in the form of SNe and stellar winds), which is similar to what we derive for the thermal energies of the hot thermal gas. This is in agreement with the detection of superstellar clusters in the starburst galaxies (see Paper I for references).

5.9 Cooling times, mass deposition rates and velocities

We derive the shortest cooling times (∼50 Myr) for NGC 3077 and He 2–10. The cooling time is much longer for NGC 1569 and 5253 (590 and 370 Myr, respectively) and NGC 4214 and 4449 fall in between (80 and 230 Myr). In general, the cooling times in the centres of the galaxies are shorter than in their outskirts (Table 6). The faster cooling towards the centres of the galaxies, however, does not result in a larger mass deposition rate $\dot{M}_{cool}$ (the rate at which the amount of coronal gas cools down). Indeed, $\dot{M}_{cool}$ is mostly lower towards the centres than towards the outer regions. This can be understood by the fact that most of the hot gas is stored in the outskirts rather than in the centres of the galaxies.

The ability of the hot gas to cool down is an important parameter for the evolution of the galaxies. Dwarf galaxies, in general, have a lower metallicity as compared with more massive spirals. The connections between the metallicities and the cooling times are shown in Fig. 9. In spite of the small difference in metallicity between most of the galaxies in the sample, a trend can be observed in the sense that the cooling is faster at larger metallicities.

The mean particle velocities fall between ∼300 and 600 km s^{-1}. Differences between velocities for the central and outer regions correlate with their temperatures. This again indicates that at a given temperature the shock velocities are approximately the same for all dwarf galaxies considered here (see Section 5.3).

6 CORRELATION OF OBSERVATIONAL PARAMETERS

Starburst galaxies are characterized by higher SFRs as compared with quiescent galaxies. The combined effect of Type II SNe and strong stellar winds then leads to the heating of the ambient medium to coronal temperatures. Consequently, SF tracers such as the Hα luminosity (from H II regions), the FIR luminosity or the blue luminosity are expected to be related to hot gas parameters. Whereas the Hα and FIR luminosities are signatures of current SF, the blue luminosity represents young stars that can live up to a few hundred

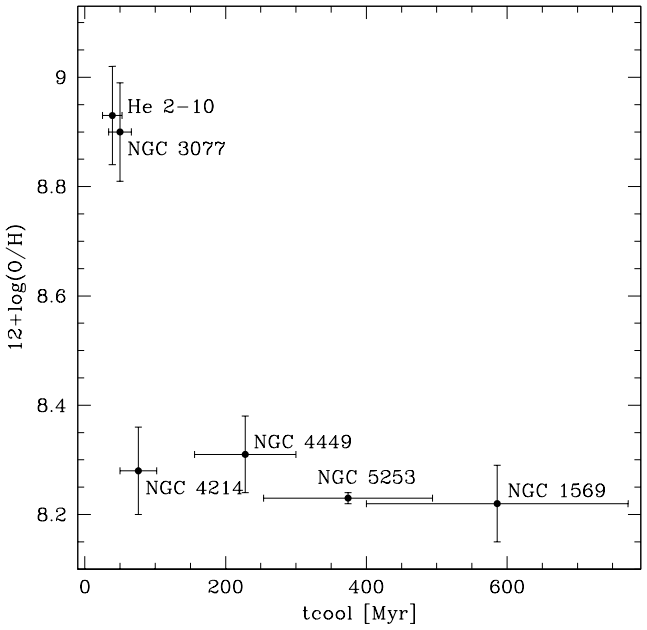

Figure 9. The H II oxygen abundances of the galaxies plotted against the cooling time of the hot gas.

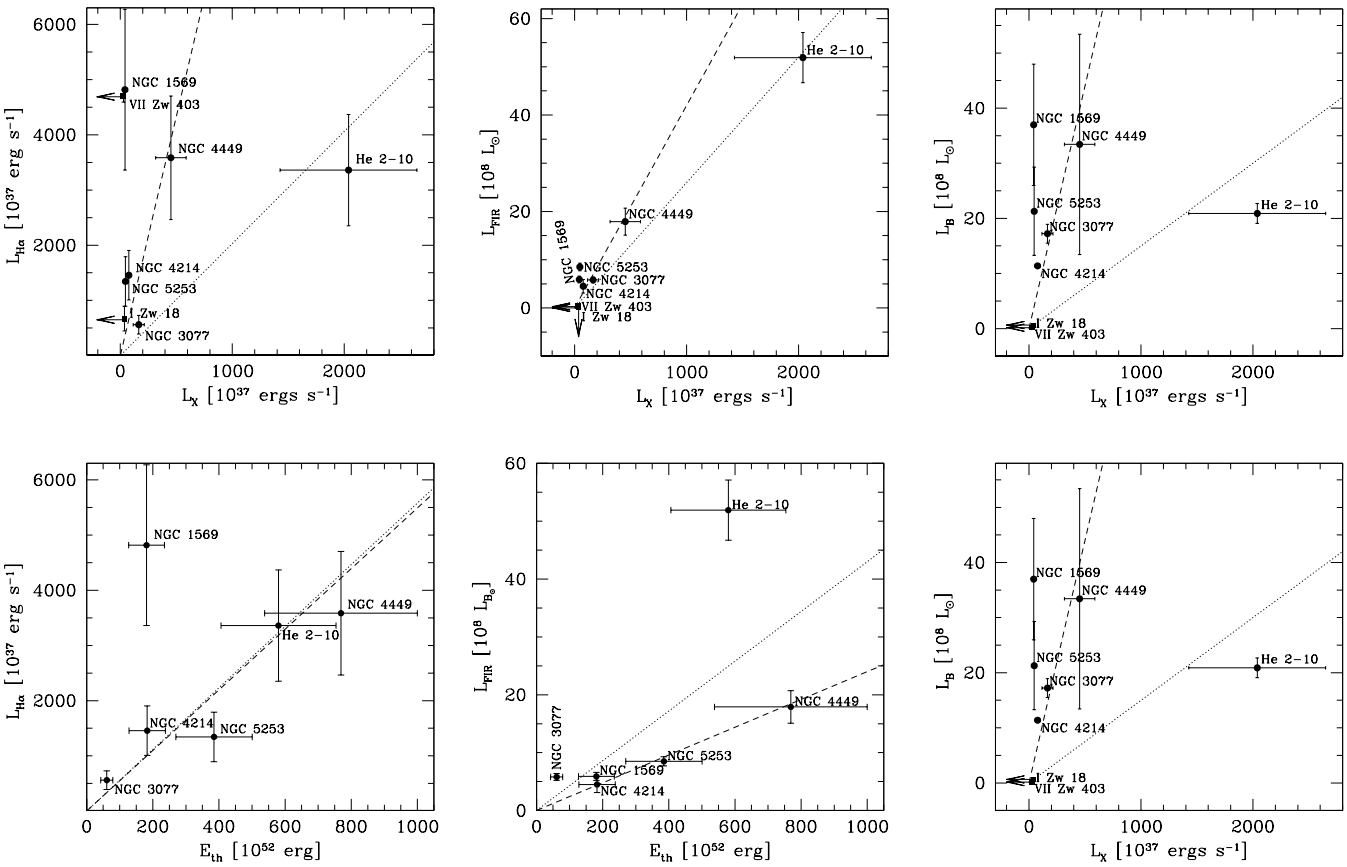

Figure 10. The star formation rate (SFR) tracers Hα , FIR emission and blue luminosity as a function of the X-ray luminosity (upper panels) and thermal energy (lower panels) of the hot gas. Least-squares fits to the graphs are plotted as dashed (dotted) lines including (excluding) He 2-10. The slopes of these fits are listed in Table 8.

Myr (e.g. Leitherer et al. 1999). It is therefore a tracer of recent rather than current SF. In Fig. 10, we show correlations of these SF tracers with the X-ray luminosity L_X of the hot gas and its thermal energy E_{th} (all fits are forced to incorporate the origin). Best results are obtained for fits excluding He 2–10 and, after converting the Hα and FIR luminosities into SFRs (see Section 2), the correlations are listed in Table 8 (note that the absorbing column density of He 2–10 listed in Table 6 is larger for the entire galaxy than for its centre and the correction for absorption might therefore overestimate its X-ray luminosity by an order of magnitude; see also the discussion in Section 4.2). In particular, the trends with both the Hα and FIR SFRs are the same within the errors. Galaxies without diffuse X-ray emission have lower blue luminosities (see also Stevens & Strickland 1998), metallicities (Fig. 7) and SFRs than those with hot gas (but see the relatively large Hα luminosity of VII Zw 403).

Note that the scatter of the Hα–L_X plot (Fig. 10, left) seems to be larger than what is suggested by the surface brightness profiles (Section 3 and Fig. 2). Both, the Hα and X-ray surface brightness profiles are very similar, which can be explained by the properties of the developing shock fronts. In Fig. 10 (left), however, the total Hα emission is shown, i.e. the H II regions and the more diffuse Hα emission. The former has been excluded from the surface brightness analysis.

The K-band luminosities of the galaxies (Table 3) may be used as a tracer for their total mass as it is dominated by low-mass and/or old stellar populations. In Fig. 11, we plot the X-ray luminosity, the thermal energy and the density of the hot gas as a function of this parameter. Some tentative trends are visible in the sense that the X-ray luminosities and the thermal energies are larger for more massive objects. Also the density of the hot gas appears to be somewhat larger with increased K-band luminosities. The parameters of the hot gas certainly depend on their ambient, gaseous medium. To check this, we plot the X-ray luminosities, the densities and the pressures of the hot gas as a function of the H I masses in Fig. 12. Here, the density again appears to be a function of the H I mass, i.e. a large H I mass is correlated with a higher density of the hot gas. As the temperatures of the hot gas are relatively uniform over the sample, this trend is also visible when plotting the pressures versus H I masses. The X-ray luminosity, however, seems not to be related to this parameter.

Table 8. Star formation (SF) tracers as a function of the X-ray luminosity L_X and the thermal energy E_{th} of the diffuse, hot gas. Shown are the fits for the sample (see Fig. 10). The quantities in the header equal the proportionality constants in the table multiplied by the quantities in the first column. Values in brackets exclude He 2–10 from the fits [$SFR_{H\alpha}$ and SFR_{FIR} are the star formation rates (SFRs) derived from Hα and far-infrared (FIR) luminosities, respectively; L_B is the blue luminosity].

	$SFR_{H\alpha}$ (10^{-4} M$_\odot$ yr^{-1})	SFR_{FIR} (10^{-4}M$_\odot$ yr^{-1})	L_B (10^5 $L_{B,\odot}$)
L_X	1.81 ± 1.10	4.48 ± 3.45	15 ± 11
(10^{37} erg s^{-1})	(7.72 ± 4.29)	(7.24 ± 1.38)	(88 ± 39)
E_{th}	1.15 ± 0.17	1.94 ± 0.64	10.4 ± 2.9
(10^{52} erg)	(1.32 ± 0.54)	(1.03 ± 0.19)	(13.4 ± 5.2)

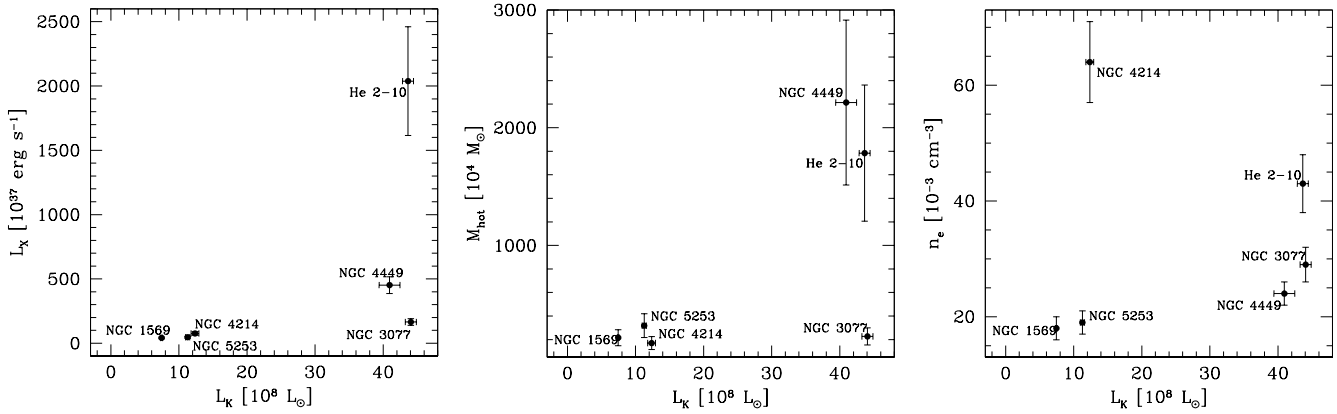

Figure 11. X-ray luminosity, mass and density of the hot gas plotted against the *K*-band luminosity of the host galaxy.

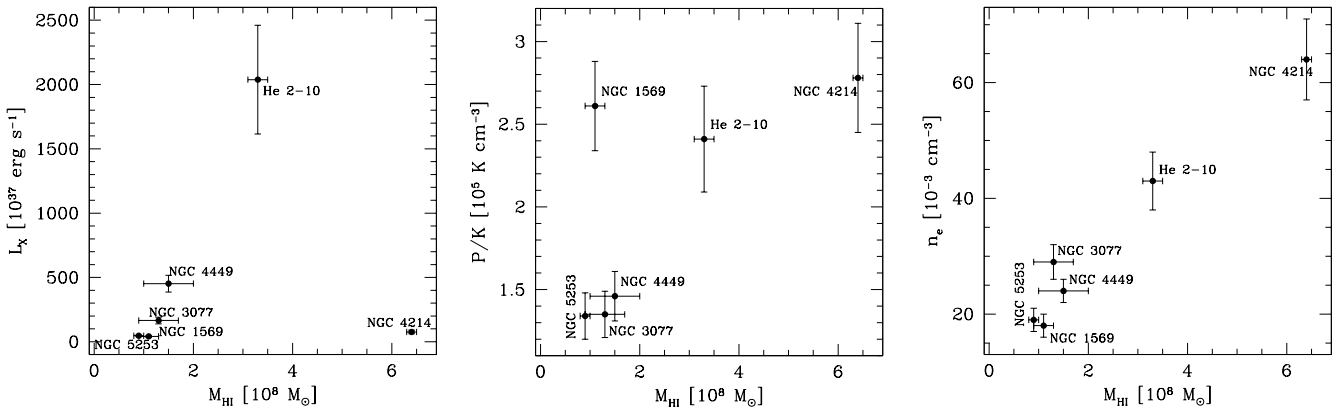

Figure 12. X-ray luminosity, pressure and density of the hot gas plotted against the H I mass of their respective hosts.

7 OUTFLOW

We will now discuss the question of whether the energetic input of SF in the galaxies may have resulted in gas removal or not. Theoretical models in the literature try to describe the conditions for this scenario (e.g. Mac Low & McCray 1988; Mac Low & Ferrara 1999; Ferrara & Tolstoy 2000; Silich & Tenorio-Tagle 2001). The escape velocity of the galaxy is a crucial parameter and has to be exceeded by any superwind in order to remove gas from the gravitational well. The escape velocity depends on the mass of the system. It is very difficult, however, to make an accurate estimate of the total dark matter content. Especially for our sample, where at least three galaxies are interacting with one or more companion galaxies (I Zw 18, NGC 3077, NGC 4449) it is virtually impossible to derive a reliable rotation curve from H I measurements, and therefore to correctly estimate the shape and depth of the gravitational potential. These galaxies are characterized by close, large tidal tails visible in H I (see Section 3). In addition, the loss of ISM can only take place if the hot gas moves supersonically when reaching the scalelength of the cooler, surrounding ISM (Silich & Tenorio-Tagle 2001). If so, the hot gas will be re-accelerated and cannot be retained by its host. If this is not the case, the gas will cool down in the halo of the galaxy and eventually rain back on its disc.

For the highly disturbed galaxies, one would need to elaborate detailed hydrodynamical simulations for a correct description of the fate of the superwinds. This, however, is beyond the scope of this paper. Instead, we discuss the probabilities for escape in the light of the model described by Silich & Tenorio-Tagle (2001; with galaxy dynamics based on Koo & McKee 1992; Mac Low & Ferrara 1999). They derive the threshold for the energy input of the starburst required to overcome the gravitational potential based on the ISM mass and the pressure of the surrounding IGM [with a scaling law for dark matter of $M_{\rm DM} = 3.47 \times 10^8 (M_{\rm ISM}/10^7\,{\rm M}_\odot)^{0.71}\,{\rm M}_\odot$]. If those thresholds are exceeded, the gas is ultimately lost to the IGM. Their results are shown in Fig. 13. Using their thresholds, the graph is split into an area where the galaxies do not suffer mass loss and an area where mass can escape to the IGM. The plotted thresholds correspond to a galaxy without rotation and is therefore an upper limit for the injected mechanical luminosity to guarantee retention of the gas; when rotation is introduced to their models, the thresholds are lowered. The dotted line in Fig. 13 was computed for an IGM pressure of $P_{\rm IGM}/k = 100\,{\rm K\,cm^{-3}}$ and the solid line for $P_{\rm IGM}/k = 1\,{\rm K\,cm^{-3}}$. We plotted the galaxies in our sample in this figure. The mechanical luminosities in Fig. 13(a) are based on Hα long-slit spectroscopy of Martin (1998; I Zw 18, NGC 1569, NGC 3077, NGC 4214, NGC 4449, NGC 5253), Méndez et al. (1999; He 2–10) and Silich et al. (2002; VII Zw 403). The mechanical luminosities derived by Martin (1998) depend linearly on the ambient density of the gas. In OMW03, densities were derived for individual superbubbles in the case of NGC 3077 and the total mechanical luminosity shown here is corrected accordingly. For the rest of the sample, we use a mean density of $0.1\,{\rm cm^{-3}}$. Note, however, that the densities of the ambient gas can be an order of magnitude higher (as in the case NGC 3077, see OMW03) and we plot the corresponding

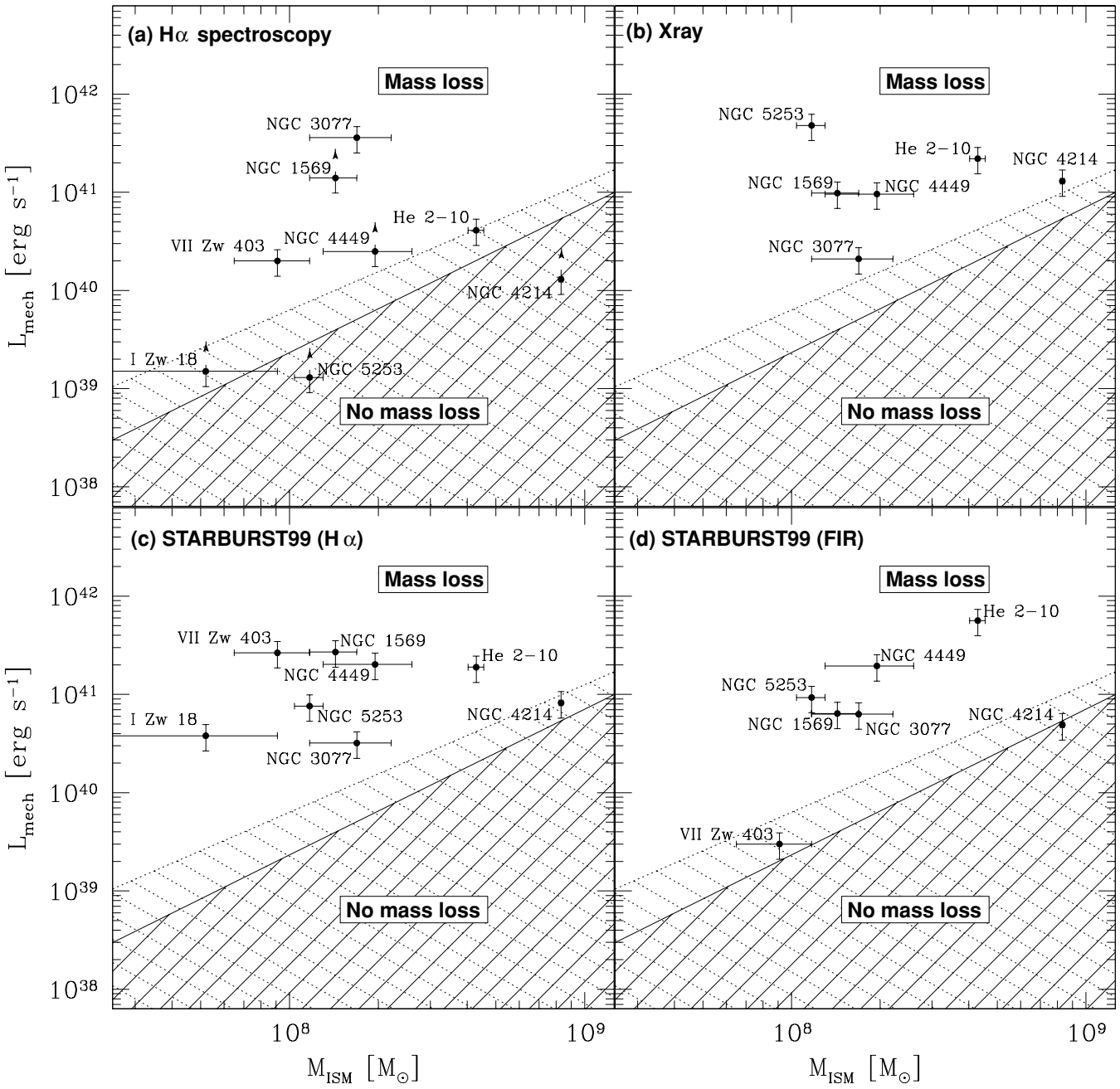

Figure 13. Mechanical luminosities of the starbursts within the galaxies as a function of their interstellar medium (ISM) mass (He corrected H I masses). Shown are theoretical thresholds taken from Silich & Tenorio-Tagle (2001) for non-rotating objects; for objects falling within the region outside of the shaded areas, material is ultimately lost to the intergalactic medium (IGM); starburst galaxies within the shaded region retain their ISM. The solid threshold was computed for an IGM pressure of $P_{\rm IGM}/k = 100\,{\rm cm}^{-3}\,{\rm K}$ and the dotted threshold for $P_{\rm IGM}/k = 1\,{\rm cm}^{-3}\,{\rm K}$. The thresholds are lower when the galaxies are rotating. Mechanical luminosities are derived from (a) Hα long-slit spectroscopy (lower limits are computed for a lower ambient gas density limit of 0.1 cm^{-3}), (b) X-ray parameters, (c) STARBURST99 models scaled by $SFR_{\rm H\alpha}$ and (d) STARBURST99 models scaled by $SFR_{\rm FIR}$.

luminosities as lower limits in Fig. 13(a). The ISM mass for all galaxies is based on the H I masses taken from Table 3 and corrected for the contribution of helium by a multiplication of 1.3. As it is difficult to correct for the amount of molecular gas, we do not account for it; if the molecular medium would be as massive as the atomic phase (an extreme scenario), the location of the points on the logarithmic scale used in Fig. 13 would shift by 0.3 to the right.

In addition to the mechanical luminosities derived by Hα spectroscopy, we estimate mechanical luminosities from our X-ray observations in a different, independent manner. The time-scale for mass injection was taken as the scalelength of the hot gas divided by the mean velocity per particle (see Tables 4 and 6). Subsequently, the thermal energies were divided by the resulting time-scales. The luminosities thus obtained are plotted as a function of ISM mass in Fig. 13(b).

Finally, we estimate the mechanical luminosities liberated by the starbursts on the basis of the STARBURST99 models (Leitherer et al. 1999, their fig. 112; see Section 5.7 for the parameters of the

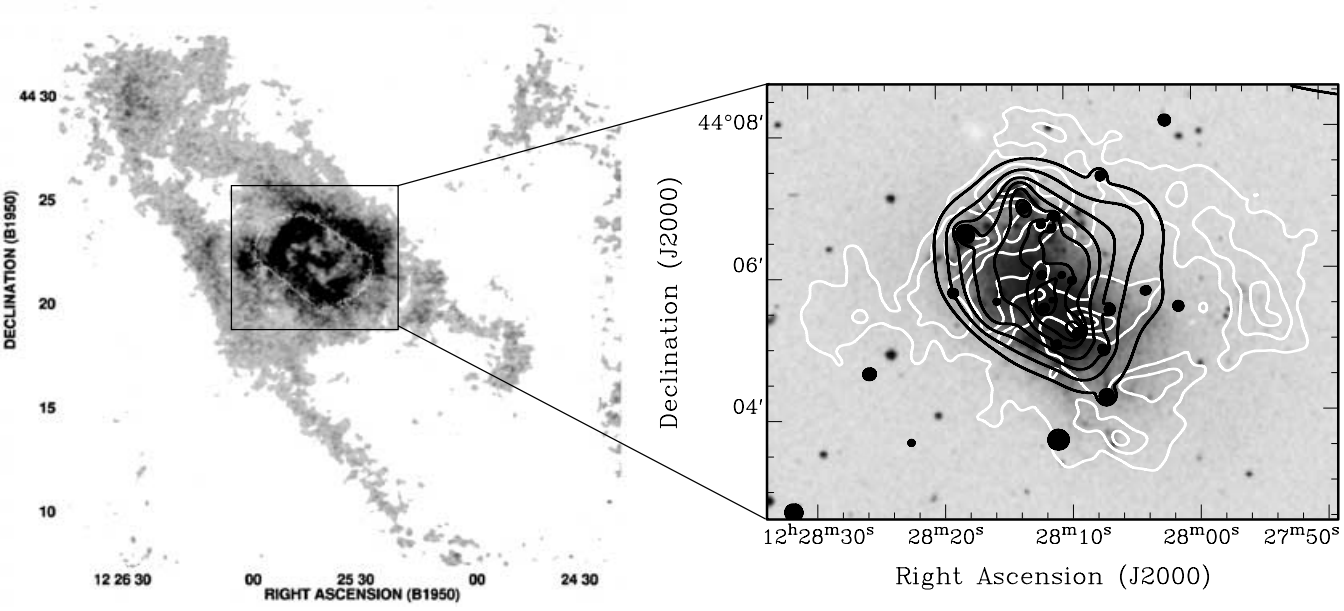

Figure 14. Left: H I map of NGC 4449 and its surrounding tidal tails. The optical counterpart is outlined as white contours. Right: optical DSS image of NGC 4449. Overlaid are contours of the H I (enlargement of left image: white) and the X-ray emission (black). The H I data were kindly provided by Hunter et al. (1999).

starburst that we adopt here). Scaling these models by the SFRs given in Table 3 and using the asymptotic solution of the STARBURST99 model (note that the mechanical luminosity stays approximately constant for starburst ages larger than the time-scale needed for the first SN to explode), we derive the mechanical luminosities displayed in panels (c) and (d) of Fig. 13. The data in Fig. 13(c) are based on the SFRs derived on the basis of Hα measurements ($SFR_{\rm H\alpha}$) and the data in Fig. 13(d) are derived for the SFRs converted from the FIR luminosities of the galaxies ($SFR_{\rm FIR}$).

Judging from the mechanical luminosities derived on the basis of Hα spectroscopy (Fig. 13a), gas loss is predicted for VII Zw 403, NGC 3077, NGC 1569 and NGC 4449. He 2–10, I Zw 18, NGC 4214 and NGC 5253 are not necessarily losing material to the halo given their energetics. Those galaxies can exceed the theoretical thresholds, however, if they rotate fast enough, the ambient densities are higher than the adopted 0.1 cm^{-3} (increasing the mechanical luminosities), or the pressure of the IGM is relatively low. According to the mechanical luminosities estimated from the diffuse X-ray emission (Fig. 13b), the starbursts in all galaxies exhibit a sufficient energy deposition rate to push the hot gas away from the galaxies independent of their rotational velocities. The results based on the STARBURST99 models yield a very similar picture and only the superwinds in NGC 4214 (and maybe VII Zw 403) might be too weak to force gas loss if their rotation is not significant. Fig. 13 therefore strongly suggests that the energy provided by the starburst is sufficient for these galaxies to develop a superwind, leading to a partial loss of the ISM. The observed overpressures of the hot gas as compared with the surroundings support this scenario (Section 5.6).

As a caveat, however, the ISM must not be very extended for gas loss to occur (see, e.g. Silich & Tenorio-Tagle 1998; D'Ercole & Brighenti 1999; Silich & Tenorio-Tagle 2001). As seen in Fig. 1, NGC 3077 and 4449 are surrounded by large tidal tails. The same is true for I Zw 18 (see the H I map of van Zee et al. 1998). Inspection of the H I and X-ray morphologies reveals that the diffuse X-ray emission of NGC 3077 is more extended towards the north than towards the south following the largest H I density gradient. Towards the south of NGC 3077, the H I column density stays constant at a level of $\sim$1.5 $\times$ 10^{21} cm^{-2} (see OMW03). Once the hot gas reaches the scalelength of the H I while maintaining supersonic speed, it will ultimately be lost. As discussed in OMW03, this is likely to happen towards the north of NGC 3077. Gas streaming to the south, however, will likely cool down before reaching the low density IGM beyond the large H I tidal tail (see also Fig. 1) unless SF continues at a high level on time-scales exceeding the cooling time.

The case of NGC 4449 is somewhat different. Its H I is distributed in a ring (mean H I column density: $\sim$5 $\times$ 10^{20} cm^{-2}) tightly surrounding the optical counterpart with tidal tails connected to the ring stretching outwards (see Figs 14 and 1). Currently, the hot gas streams into the interior of the ring, which is the region of lowest H I column density. Depending on how much material can accumulate in this region before the hot gas cools down, the superwind may break through this wall. Even if the hot gas extends further out, it still has to provide the work needed to push the gas aside that is stored in the tidal tails. An escape along the line of sight is possibly not a solution as even within the ring low density H I emission is being observed over a large velocity range (Hunter, van Woerden & Gallagher 1999; see also Summers et al. 2003).

No current interaction or apparent tidal tails are observed for NGC 4214. Even though the hot gas is concentrated in the central region (see Fig. 1), it is very likely that the hot gas escapes along the line of sight, which corresponds more or less to the z-axis of this object (note the relatively face-on appearance of NGC 4214).

In summary, dwarf galaxies have the potential to release metals to the IGM in the form of powerful galactic superwinds. This is corroborated by their large mechanical energy inputs in a relatively shallow gravitational potential as well as by the overpressures of the hot gas. The main trigger for starbursts, however, is galaxy–galaxy interactions, which produce extended tidal tails, and any low density neutral envelope may provide a barrier for outflow to occur, containing the gas for times larger than the cooling time-scale and thus preventing the complete loss of ISM to the IGM.

8 SUMMARY

In Paper I, we presented a detailed discussion of the individual X-ray properties as observed with the *CXO* of a sample of eight dwarf galaxies that are in a starburst phase: I Zw 18, VII Zw 403, NGC 1569, NGC 4214, NGC 4214, NGC 4449, NGC 5253 and He 2-10. Here, we present an intercomparison of their X-ray properties as well as comparisons with observations at other wavelengths. Our results can be summarized as follows.

(i) X-ray point sources (detected within the optical or H I extent of an individual galaxy) are mainly observed close to the centres of the galaxies; only a few of them are found in their outer regions. In general, they are located close to bright H II regions, the rims of expanding superbubbles, or UV bright young stellar clusters. The type of X-ray emission mechanism model (PL, TP, or BB) of the point sources appears to be unrelated to their location.

(ii) The number of point sources correlates with the SF rates of the galaxies and, with less significance, with their blue luminosities. The cumulative luminosity function of the point sources exhibits a very shallow PL index of 0.24. This value is approximately a factor of 2–4 lower than that of more massive starbursts and approximately 6 times lower than that of non-starburst galaxies. 10 ULXs (X-ray luminosities $> 10^{39}$ erg s^{-1}) are detected in three galaxies (I Zw 18, NGC 4449, He 2–10). Each of these galaxies is part of a current interaction or merger.

(iii) Diffuse X-ray emission emerging from the coronal gas in superwinds is detected in six out of eight galaxies. The non-detection in I Zw 18 and VII Zw 403 can be understood as being a result of their smaller sizes and/or their extremely low metallicities as compared with the other galaxies in the sample. We cannot rule out that any hot gas that might have been there at earlier times has either vented into the halo or has cooled so as to become undetectable.

(iv) Superwinds traced by the diffuse, coronal gas develop along the steepest declining gradient in the ISM as observed in H I. A higher temperature is observed in the centres of the galaxies as compared with that in their outskirts. For approximately half of the sample, the X-ray emission extends well beyond the H I component, whereas in the other half the hot gas appears to be still enclosed in an H I envelope. On a global scale, the azimuthally averaged Hα and X-ray surface brightness profiles are very similar and are well fitted by exponential functions with scalelengths $\sim$100–200 pc (NGC 4449: $\sim$550 pc). This may be due to the fact that on global scale photoionization and shocks of the Hα features as well as the thermalization of the X-ray emitting gas are all the result of the impact of massive stars on the ISM distributed over the discs of the starburst galaxies. On local scales, the X-ray and Hα emission are either slightly offset or show the morphology of expanding Hα shells filled with coronal gas.

(v) Volume densities of the hot gas are in the range 0.02–0.06 cm^{-3}, pressures vary within 1–3 $\times$ 10^5 K cm^{-3}, thermal energies are $\sim$2–30 $\times$ 10^{54} erg and masses 2–20 $\times$ 10^6 M$_\odot$. Thus, compared with their H I content, approximately 1 per cent of the ISM is in the form of hot, coronal gas. The pressures involved are higher than those for the other components of the ISM. This is the most likely force driving the expansion. Mass loading of a factor of 1–5 is needed for the galaxies.

(vi) The X-ray luminosities and the cooling times of the hot gas appear to be related to the metallicities of their host galaxies. Low-metallicity objects have longer cooling times. Furthermore, galaxies with the largest mass-loading factors exhibit the shortest cooling times and the highest mass deposition rates.

(vii) Correlations are found for the H I mass of the galaxies with the pressures and densities of the hot gas. These parameters appear to increase with increasing H I mass, the hydrodynamics of which appear to control the confinement of the hot gas. Such a correlation is only tentatively visible when plotting the hot gas parameters against the *K*-band luminosities (used as a tracer for total mass of the galaxies). In addition, the X-ray luminosities and thermal energies of the hot gas may be used to trace star formation in the galaxies. A larger sample, however, is needed to strengthen this correlation.

(viii) The mechanical energies, as derived from Hα and X-ray observations, are large enough to overcome the gravitational potential of their hosts. In combination with the fact that the current SF is still high and that the hot gas shows an overpressure compared with the ambient ISM, we conclude that outflows are likely and that the hot, α elements enriched gas component is lost to the IGM. When large-scale, low density H I tidal tails are present, however, the hot gas appears to be confined within those tidal structures.

Dwarf galaxies that are undergoing a starburst are important objects to study as a result of their potential contribution to the metal enrichment of the IGM at large look-back times. The number of dwarf galaxies in the Universe may be large enough to move significant amounts of matter (and thus metals) to the IGM. Here, we have shown that outflows are possible in a number of nearby dwarf starbursts; however, some fraction of galaxies will retain their hot gas as a result of the hydrodynamical drag of extended envelopes of cooler material. Deeper observations of a larger sample of dwarf (starburst) galaxies will be necessary to determine if and in which proportion these objects contribute to the metal enrichment of the Universe.

ACKNOWLEDGMENTS

We would like to thank Dominik Bomans, John Cannon, Deidre Hunter, Chip Kobulnicky, Vince McIntyre and Stefanie Mühle for providing optical, Hα and H I images of the galaxies. In particular, we thank Crystal Martin for providing some optical images as well as for valuable discussions on NGC 3077 and He 2–10. We are also grateful to David Strickland for the critical reading of the manuscript. JO acknowledges the Graduiertenkolleg 118 'The Magellanic System, Galaxy Interaction, and the Evolution of Dwarf Galaxies' of the Deutsche Forschungsgemeinschaft (DFG). EB is grateful to CONACyT for financial support through grant 27606-E. This research has made use of the National Aeronautics and Space Administration (NASA)/IPAC Extragalactic Data base (NED) and the NASA/IPAC Infrared Science Archive, which are maintained by the Jet Propulsion Laboratory, Caltech, under contract with NASA, the NASA Astrophysical Data System Abstract Service (ADS), the NASA SkyView and the astronomical data base SIMBAD, provided by the 'Centre de Données astronomiques de Strasbourg' (CDS).

REFERENCES

Beichman C. A., Neugebauer G., Habing H. J., Clegg P. E., Chester T. J., 1988, NASA Reference Publication, 1190, 1
Bottinelli L., Gouguenheim L., Fouque P., Paturel G., 1990, A&AS, 82, 391
Cannon J. M., Skillman E. D., Garnett D. R., Dufour R. J., 2002, ApJ, 565, 931
Castor J., Weaver R., McCray R., 1975, ApJ, 200, L107
Chevalier R. A., Clegg A. W., 1985, Nat, 317, 44
Colbert E. J. M., Ptak A. F., 2002, ApJS, 143, 25
Conti P. S., Vacca W. D., 1994, ApJ, 423, L97

Cox A. N. 2000, Allen's Astrophysical Quantities, 4th edn. AIP Press, New York
Crawford D. F., Jauncey D. L., Murdoch H. S. 1970, ApJ, 162, 405
D'Ercole A., Brighenti F., 1999, MNRAS, 309, 941
Ferrara A., Tolstoy E., 2000, MNRAS, 313, 291
Freedman W. L. et al., 1994, ApJ, 427, 628
Frei Z., Guhathakurta P., Gunn J. E., Tyson J. A., 1996, AJ, 111, 174
Gibson B. K. et al., 2000, ApJ, 529, 723
Grimm H.-J. Gilfanov M., Sunyaev R. 2003, MNRAS, 339, 793
Guseva N. G., Izotov Y. I., Thuan T. X., 2000, ApJ, 531, 776
Heckman T. M., 2002, in Mulchaey J. S., Stocke J., eds, ASP Conf. Ser. Vol. 254, Extragalactic Gas at Low Redshift. Astron. Soc. Pac., San Francisco, p. 292
Heckman T. M., Lehnert M. D., Armus L., 1993, in Shull J. M., Thronson H. A., Jr, eds, ASSL Vol. 188, The Environment and Evolution of Galaxies. Kluwer, Dordrecht, p. 455
Huchtmeier W. K., Richter O.-G., 1989, A General Catalog of HI Observations of Galaxies. The Reference Catalog, XIX. Springer–Verlag, Berlin, Heidelberg, New York, p. 350
Huchtmeier W. K., Seiradakis J. H., 1985, A&A, 143, 216
Huchtmeier W. K., Sage L. J., Henkel C., 1995, A&A, 300, 675
Hunter D. A., Gillett F. C., Gallagher J. S., Rice W. L., Low F. J., 1986, ApJ, 303, 171
Hunter D. A., Hawley W. N., Gallagher J. S., 1993, AJ, 106, 1797
Hunter D. A., Wilcots E. M., van Woerden H., Gallagher J. S., Kohle S., 1998, ApJ, 495, L47
Hunter D. A., van Woerden H., Gallagher J. S., 1999, AJ, 118, 2184
Israel F. P., 1988, A&A, 194, 24
Izotov Y. I., Thuan T. X., Lipovetsky V. A., 1997, ApJS, 108, 1
Jarrett T. H. Chester T., Cutri R. Schneider S. E., Huchra J. P. 2003, AJ, 125, 525
Johnson K. E., Leitherer C., Vacca W. D., Conti P. S., 2000, AJ, 120, 1273
Kaaret P., Alonso-Herrero A., Gallagher J. S., Fabbiano G., Zezas A., Rieke M. J., 2004, MNRAS, 348, L28
Kaastra J. S., 1991, An X-Ray Spectral Code for Optically Thin Plasmas. Internal SRON–Leiden Report, updated version 2.0
Kennicutt R. C., 1983, ApJ, 272, 54
Kennicutt R. C., 1998, ApJ, 498, 541
Kilgard R. E., Kaaret P., Krauss M. I., Prestwich A. H., Raley M. T., Zezas A., 2002, ApJ, 573, 138
King A. R., 2004, MNRAS, 347, L18
Kobulnicky H. A., Skillman E. D., 1995, ApJ, 454, L121
Kobulnicky H. A. Skillman E. D., 1996, ApJ, 471, 211
Kobulnicky H. A., Dickey J. M., Sargent A. I., Hogg D. E., Conti P. S., 1995, AJ, 110, 116
Kobulnicky H. A., Kennicutt R. C., Pizagno J. L., 1999, ApJ, 514, 544
Koo B., McKee C. F., 1992, ApJ, 388, 93
Lambert D. L., 1978, MNRAS, 182, 249
Lang K. R., 1992, Astrophysical data: planets and stars. Springer–Verlag, Heidelberg
Lauberts A., Valentijn E. A., 1989, The surface photometry catalogue of the ESO–Uppsala galaxies. European Southern Observatory, Garching
Liedahl D. A., Osterheld A. L., Goldstein W. H., 1995, ApJ, 438, L115
Leitherer C. et al., 1999, ApJS, 123, 3
Lynds R., Tolstoy E., O'Neil E. J., Hunter D. A., 1998, AJ, 116, 146
Mac Low M., Ferrara A., 1999, ApJ, 513, 142
Mac Low M., McCray R., 1988, ApJ, 324, 776
Maíz-Apellániz J., Cieza L., MacKenty J. W., 2002, AJ, 123, 1307
Marlowe A. T., Heckman T. M., Wyse R. F. G., Schommer R., 1995, ApJ, 438, 563
Marlowe A. T., Meurer G. R., Heckman T. M., Schommer R., 1997, ApJS, 112, 285
Martin C. L., 1996, ApJ, 465, 680
Martin C. L., 1997, ApJ, 491, 561
Martin C. L., 1998, ApJ, 506, 222
Martin C. L., Kobulnicky H., Heckman T. 2002, ApJ, 574, 663
Matteucci F., Recchi S., 2001, ApJ, 558, 351
Méndez D. I., Esteban C., Filipović M. D., Ehle M., Haberl F., Pietsch W., Haynes R. F., 1999, A&A, 349, 801
Mewe R., Gronenschild E. H. B. M., van den Oord G. H. J., 1985, A&AS, 62, 197
Mühle S. 2003, PhD thesis, Univ. of Bonn
Östlin G., 2000, ApJ, 535, L99
Ott J., Martin C. L., Walter F., 2003, ApJ, 594, 776 (OMW03)
Ott J., Walter F., Brinks E., 2005, MNRAS, in press (doi: 10.1111/j.1365-2966.2005.08862.x) (Paper I, this issue)
Paturel G. et al., 1997, A&AS, 124, 109
Raymond J. C., Smith B. W., 1977, ApJS, 35, 419
Rohlfs K., Wilson T. L., Hüttemeister S., 2000, in Rohlfs K., Wilson T. L., eds, Tools of radio astronomy. Springer, New York, p. 321 (Astronomy and astrophysics library, ISSN0941-7834)
Sauvage M., Thuan T. X., Lagage P. O., 1997, A&A, 325, 98
Silich S. A., Tenorio-Tagle G., 1998, MNRAS, 299, 249
Silich S. A., Tenorio-Tagle G., 2001, ApJ, 552, 91
Silich S. A., Tenorio-Tagle G., Terlevich R., Terlevich E., Netzer H., 2001b, MNRAS, 324, 191
Silich S., Tenorio-Tagle G., Muñoz-Tuñón C., Cairos L. M., 2002, AJ, 123, 2438
Skillman E. D., Kennicutt R. C., Hodge P. W., 1989, ApJ, 347, 875
Soifer B. T., Boehmer L., Neugebauer G., Sanders D. B., 1989, AJ, 98, 766
Solomon P. M., Downes D., Radford S. J. E., Barrett J. W., 1997, ApJ, 478, 144
Stevens I. R., Strickland D. K., 1998, MNRAS, 294, 523
Strickland D. K., Stevens I. R., 2000, MNRAS, 314, 511
Strickland D. K., Heckman T. M., Weaver K. A., Hoopes C. G., Dahlem M., 2002, ApJ, 568, 689
Summers L. K., Stevens I. R., Strickland D. K., Heckman T. M., 2003, MNRAS, 342, 690
Sutherland R. S., Dopita M. A., 1993, ApJS, 88, 253
Theis C., Kohle S., 2001, A&A, 370, 365
Tully R. B., Boesgaard A. M., Dyck H. M., Schempp W. V., 1981, ApJ, 246, 38
Vacca W. D., Conti P. S., 1992, ApJ, 401, 543
Walter F., Taylor C. L., Hüttemeister S., Scoville N., McIntyre V., 2001, AJ, 121, 727
Walter F., Weiss A., Martin C., Scoville N., 2002, AJ, 123, 225
Weaver R., McCray R., Castor J., Shapiro P., Moore R., 1977, ApJ, 218, 377
Wolfire M. G., McKee C. F., Hollenbach D., Tielens A. G. G. M., 2003, ApJ, 587, 278
Yun M. S., Ho P. T. P., Lo K. Y., 1994, Nat, 372, 530
van Zee L., Westpfahl D., Haynes M. P., Salzer J. J., 1998, AJ, 115, 1000
Zezas A., Fabbiano G., 2002, ApJ, 577, 726

This paper has been typeset from a TEX/LATEX file prepared by the author.